

What's Behind the Couch? Directed Ray Distance Functions (DRDF) for 3D Scene Reconstruction

Nilesh Kulkarni

Justin Johnson

David F. Fouhey

University of Michigan

{nileshk, justincj, fouhey}@umich.edu

Abstract

We present an approach for scene-level 3D reconstruction, including occluded regions, from an unseen RGB image. Our approach is trained on real 3D scans and images. This problem has proved difficult for multiple reasons; Real scans are not watertight, precluding many methods; distances in scenes require reasoning across objects (making it even harder); and, as we show, uncertainty about surface locations motivates networks to produce outputs that lack basic distance function properties. We propose a new distance-like function that can be computed on unstructured scans and has good behavior under uncertainty about surface location. Computing this function over rays reduces the complexity further. We train a deep network to predict this function and show it outperforms other methods on Matterport3D, 3D Front, and ScanNet.

1. Introduction

Consider the top-left of Figure 1. What happens if you step to the right and look behind the chair? To you, this single image represents a rich 3D world in which the cabinet continues behind the chairs. This work aims to learn a mapping from a single image to a 3D reconstruction of a scene, including visible *and* occluded surfaces, while learning from real, unstructured scans like Matterport3D [5] or ScanNet [10]. These non-watertight scans are currently one of the richest sources of real-world 3D ground truth, and as more devices integrate LIDAR scanners, their importance will only grow.

Learning from these scans poses challenges to current computer vision methods. Representations based on voxels [9, 18] scale poorly with size, and meshes [54] struggle with widely varying topology. Implicit functions [35, 40] have shown promise at overcoming the size and topology issues of meshes and voxels. However, most work has focused on watertight meshes [7, 35, 38, 40, 45] where there is a well-defined inside and outside. Watertightness



Figure 1. Our approach generates 3D from a single unseen image (left) while training on real 3D scans. We show the two rendered novel views of our method’s output (middle, right). Visible surfaces are colored by the image and occluded ones are colored with surface normals: **pink** is upwards and **lavender** faces the camera. We can observe the occluded cabinet and floors behind the couch.

enables using *signed distance functions* (SDF) or occupancy functions, but limits methods to watertight data like ShapeNet [6], humans [40], or memorizing single watertight scenes [45]. Real 3D scans (e.g., [5, 10]), on the other hand are off-limits. Exceptions include [8], which fits an *unsigned distance function* (UDF) to instance-specific models, and SAL [1, 2] which learns SDFs on objects with well-defined insides and outsides that also have holes.

We believe the lack of success on learning to predict implicit functions on datasets like Matterport3D [5] stems from three key challenges. First, the unstructured, scene-level nature of the 3D data precludes functions like the SDF or occupancy: even if one starts with watertight surfaces, clipping with the view frustum can make the SDF poorly defined. Second, the distance function to a scene can depend on large parts of the image: as a ray goes through the scene, the nearest point often wanders around, producing a complex distance function. Finally, predicted distance function from models in our settings are *not* characteristics of real distance functions. Instead, we show that the uncertainty about a surface location creates incentives for a model’s output to violate basic properties of distance functions, hampering surface extraction.

We propose an approach (§3) for this task, including a new distance-like function, named the *Directed Ray Distance Function* (DRDF). The DRDF can be computed on unstructured scans, does not assume the underlying mesh

is watertight, and depends only on points on a ray through a pixel. The DRDF’s behavior near an intersection is relatively stable under uncertainty (§3.3), and a simple zero-crossing (plus a sign check) can find surfaces.

We learn to predict the DRDF with a PixelNerf [56]-style architecture. We compare our proposed approach, DRDF, with other distance functions and ways of obtaining a reconstruction of the scene, such as Layered Depth Images (LDI)[44]. Our experiments (§4) compare the approaches on Matterport3D [5], 3DFront [17], and ScanNet [10]. Our evaluations show that the DRDF is substantially better at recovering the full 3D scene across a variety of metrics, including both visible and invisible regions.

2. Related Work

Our approach aims to infer the full 3D structure of a scene from a single image using implicit functions, which connects with many tasks in 3D computer vision.

Scenes from a Single Image. Reconstructing the 3D scene from image cues is a long-term goal of computer vision. Most early learning-based work focuses on 2.5D properties [4] that are visible in the image, such as qualitative geometry [15, 24], depth [42] and normals [16]. Our work instead aims to infer the full 3D of the scene, including invisible parts. Most work on invisible surfaces focuses on single objects with voxels [9, 18, 21], point-clouds [14, 32], CAD models [26] and meshes [19, 20]. These approaches are usually trained with synthetic data, e.g., ShapeNet [6] or images that have been aligned with synthetic ground-truth 3D [48]. The existing scene-level work, e.g., [30, 31, 37, 51] trains on synthetic datasets containing pre-individuated, watertight objects like SunCG [46]. Our work instead can be learned on real 3D like Matterport3D [5]. On a different front, our work is part of a larger trend in aiming to understand the interplay between 3D, uncertainty, and learning [3, 28, 39]; this work has largely been applied in the depth-map space.

Implicit Functions for 3D reconstruction. We approach the problem with using implicit functions [7, 35, 38], which have shown promise in handling problems of scale and varying topology. These implicit functions have also been used in view synthesis [34, 36, 56, 57], which differs from our work in goals. In reconstruction, implicit functions have shown impressive results on two styles of task: fitting to a single model/scene (e.g., SIREN [45]) and predicting new single objects (e.g., PiFu [40, 55]). Our work falls in the latter category as it predicts previously unseen scenes. While implicit functions have shown impressive results on humans [40, 41] and ShapeNet objects [55], most existing work relies on watertight meshes. Our non-watertight setting is more challenging, and two solutions have been proposed: assuming the existence of the SDF and supervising

it indirectly (SAL: [1, 2]), and training with an unsigned distance function (UDF) [8] (although we stress that [8] does not predict scene-level distance functions from RGB images). The DRDF can also be trained on non-watertight meshes, but outperforms these two approaches: the DRDF works even if the SDF is not defined, and is relatively stable under uncertainty.

Recovering Occluded Surfaces. Our system produces the full 3D structure of a scene, including occluded parts from a single image. This topic has been of great interest to the community (in addition to previously mentioned work on volumetric 3D e.g., [9, 18]). Early work often used vanishing-point-aligned box [12, 23] trained on annotated data. While our approach predicts floors, this is learned, not explicitly baked in, unlike modern inheritors that have explicit object and layout components [27, 50] or the ability to query for two layers [25]. One alternate approach is layered depth images (LDI) [13, 44] or multi-plane depthmaps. LDIs can be learned without direct supervision [52], but when LDIs are trained directly, they fare worse than DRDF.

3. Method

We aim to reconstruct the full 3D extent of a previously unseen scene from a single RGB image, including occluded portions and while training on real scene captures [5]. This setting is challenging because: the meshes are not watertight; scene distance functions are hard to model; and uncertainty about the surface rewards the network for distorted outputs that lack *critical* distance function properties.

We propose a new distance-like function, the *Directed Ray Distance Function (DRDF)*, that performs well in our setting and couple it with a deep network to predict it. Our method starts with a network that predicts distance functions using pixel-aligned features (§3.1). Our network is generic and can be paired with a distance function (e.g., SDF) and a decoding strategy (e.g., find zero-crossings). The choice of distance function and decoding is critical: our DRDF (§3.2) can be computed on non-watertight objects and has better properties under uncertainty (§3.3).

3.1. Setting and Base Architecture

Our goal is to learn an image-conditioned mapping from a 3D point \mathbf{x} to a (potentially signed) distance to the scene surfaces, or $f_\theta(\mathbf{x}; I) : \mathbb{R}^3 \rightarrow \mathbb{R}$. We shown an overview of approach in Fig. 2. We use a PixelNerf [56]-style architecture consisting of a backbone $b_\theta(\cdot)$ and MLP regressor $h(\cdot)$ that are jointly trained. The backbone produces a feature map \mathbf{B} , and the MLP uses \mathbf{B} along with a query point $\mathbf{x} \in \mathbb{R}^3$ to predict a distance function. We extract a feature vector $v(\mathbf{x}, \mathbf{B})$ from \mathbf{B} via bi-linear interpolation. This feature consists of the image feature at the projection of \mathbf{x} using the camera π and is concatenated with positional em-

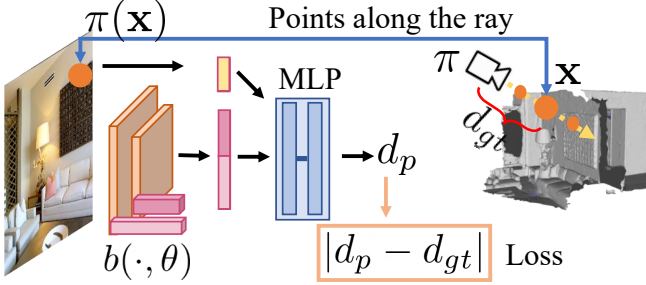


Figure 2. Approach. At training time, our model takes an image and set of 3D points along rays and is supervised on the distance to the nearest intersection via the real 3D geometry. For inference, our model predicts the distance for each point in a 3D grid, which is then decoded to intersections. More details under §3.1

embedding [36] of \mathbf{x} . The final prediction d_p is made by a MLP regressor head $h_\theta(v(\mathbf{x}, B))$, making the full output of $f_\theta(\mathbf{x}; I)$ equal to $h_\theta(v(\mathbf{x}, b_\theta(I)))$.

At training time, we are given n samples $\{(\mathbf{x}_i, I_i, d_i)\}_{i=1}^n$, each consisting of an image I_i , point \mathbf{x}_i , and target distance d_i . We find the minimizer θ^* of the empirical risk $\sum_{i=1}^n \mathcal{L}(f_\theta(\mathbf{x}_i, I_i), d_i)$ for a loss \mathcal{L} . By changing the targets d_i , one can change distance functions.

At test time, one predicts the distance at a set of points in 3D, which in turn must be *decoded* into a set of surface locations. Given a ground truth distance function, this decoding is usually a trivial post-processing and one can use any number of properties of distance functions (e.g., the presence of a zero-crossing in value or its derivative) to obtain a surface. However, in our setting with uncertainty, we find the choice of distance function is important. Our proposed approach is well-behaved under uncertainty, and so its decoding is trivial and hyper-parameter free, but we extensively optimize the decoding strategies of baseline methods.

3.2. Distance Functions

It is critical to distinguish between *scene distance functions* and *ray distance functions*. Given a point \mathbf{x} , the scene distance considers the distance between \mathbf{x} and all points in the scene. For example, given a set of 3D points \mathcal{P} , the *unsigned distance function* (UDF) is the distance to the nearest point in the scene, $d_U(\mathbf{x}) = \min_{\mathbf{x}' \in \mathcal{P}} \|\mathbf{x} - \mathbf{x}'\|_2$. A ray distance, on the other hand, only considers the points in \mathcal{P} along the ray joining \mathbf{x} and the camera center (assumed to be $\mathbf{0}$), or $\{\mathbf{sx} : s \in \mathbb{R}^+, \mathbf{sx} \in \mathcal{P}\}$. Ray distance functions can be constructed by applying a standard distance function to the 1D space along the ray. Suppose \mathcal{D} is set of *distances* to surfaces the ray through \mathbf{x} crosses, or $\mathcal{D} = \{s : s \in \mathbb{R}^+, \mathbf{sx} \in \mathcal{P}\}$. Then, given a distance z along the ray, the *unsigned ray distance function* (URDF) $d_{UR}(z)$ is defined as $\min_{s \in \mathcal{D}} |z - s|$. The URDF is precisely the 1D case of the UDF applied to distances along the ray.

Considering only the ray through a pixel has conse-



Figure 3. Scene vs. ray distances. (a) A 2D cross-section of a simplified kitchen. The red ray intersects the scene at the black and white points along the ray. These points define the *ray distance*. However, the nearest points on the ray in the scene (colored by distance Min — Max) cover the nearly the full scene. These far-flung points define the *scene distance*. We shade this area in light blue. (b) A real 3D example of a different scene. The colored points project all over the scene.

quences for learning to predict distances. By definition, the only surfaces in the scene that define a ray distance function are also on the ray to \mathbf{x} ; these surfaces thus also project to the same location as \mathbf{x} . In contrast, the set of surfaces that defines a scene distance can fall all over the scene. We illustrate this in Fig. 3. Given the set of points along ray through \mathbf{x} , or $\{\mathbf{sx} : s \in \mathbb{R}^+\}$, we can compute the set of scene points that are nearest to a point on the ray, or $\{\arg \min_{\mathbf{x}' \in \mathcal{P}} \|\mathbf{sx} - \mathbf{x}'\|_2 : s \in \mathbb{R}^+\}$. The projection of this is usually large. We can compute the set of scene points that are nearest to a point on the ray or This set of points usually projects to all over the image. We quantify this by measuring how far the projection of all the nearest points is from the ray center. The largest distance gives the minimum distance the network needs to look. The average maximum distance from ray center is 96px on a 256²px image (averaged over 50K rays on Matterport3D [5]). The network might also need to look and examine all the points within 1m of the ray. This requires looking 145px away from the ray on an average. Thus, accurately inferring a UDF often requires a network to integrate information from much more of the image compared to a ray distance function.

Focusing on rays, we can define more ray distance functions. For watertight meshes, one can have a predicate *inside(z)* that is 1 when z is *inside* an object; then the *Signed Ray Distance Function* (SRDF) is $d_{SR}(z) = -\text{inside}(z) \min_{s \in \mathcal{D}} |z - s|$. Since our setting is non-watertight, the SRDF is impossible, as is using *inside* to define occupancy. However, one can define a proximity-based occupancy ray function (ORF) that is 1 if z is within r of an intersection $d_{ORF}(z) = (\min_{s \in \mathcal{D}} |z - s|) < r$.

We introduce a new ray distance-like function, called the *Directed Ray Distance Function*. Given a set of intersections \mathcal{D} along the ray and distance z , the DRDF is $d_{DRDF}(z) = (\arg \min_{s \in \mathcal{D}} |s - z|) - z$. Like the URDF, there

is no notion of inside, so the DRDF can be used with unstructured scans. Near an intersection, the DRDF behaves like the SDF and crosses zero. In exchange, there is a sharp discontinuity halfway between intersections.

3.3. Distance Functions Under Uncertainty

When a network is trained on one unambiguous scene, its optimal output is to reproduce the scene perfectly. We now ask what happens with uncertainty, e.g., if a network predicts a new scene from an RGB image. We analyze the uncertainty of a single intersection, which we now assume is a random variable S rather than a fixed location. In this case, the ray distance function depends on what value s the random variable S takes on. We denote the distance function at z if the intersection is at s as $d(z; s)$.

Under uncertainty, a network trained to minimize the MSE is optimal when it produces the expected distance under S , or $E_S[d(z; s)] = \int_{\mathbb{R}} d(z; s)p(s)ds$ where $p(s)$ is the density of S . This expectation minimizes other losses: if $d(z; s)$ is an indicator, $E_S[d(z; s)]$ minimizes the cross-entropy loss; and if the distribution over distances to S is symmetric, then $E_S[d(z; s)]$ also minimizes the L1 loss.

We can understand optimal behavior under uncertainty for a given form of S by calculating $E_S[d(z; s)]$ for different ray distance functions. We derive results for when S is normally distributed with its mean μ at the true intersection, standard deviation σ , and CDF $\Phi(s)$. Since distance functions also depend on the next intersection, we assume the next intersection is at $S + n$ for a constant $n \in \mathbb{R}^+$.

We summarize some salient results here, and a detailed analysis appears in the supplement. No expected function perfectly matches its true function, but each varies in where the distortion occurs. Figure 4 shows $E_S[d(z; s)]$ for three ray distance functions (for $n = 1, \sigma = 0.2$). At the intersection, the expected SRDF and DRDF closely match the true function while the expected URDF is grossly distorted. Full derivations appear in the supplemental, but the expected URDF has a minimum value of $\approx \sigma\sqrt{2/\pi}$ rather than 0. Similarly, its previously sharp derivative is now now $\approx 2\Phi(z) - 1$, which is close to ± 1 only when z is far from the intersection. In contrast, the expected DRDF's distortion occurs at $\mu + \frac{n}{2}$, and its derivative $(np(z - \frac{n}{2}) - 1)$ is close to -1 , except when z is close to $\mu + \frac{n}{2}$.

These distortions disrupt decoding of distance functions to surfaces. An actual URDF can be converted to a surface by thresholding, but the expected URDF has minimum value $\approx \sigma\sqrt{2/\pi}$, not 0. In 3D estimation, the errors are usually heteroscedastic, e.g., a nearby intersection often has less uncertainty than a far intersection (even just because the error is relative). So a threshold that handles certain (e.g., near) intersections may miss uncertain (e.g., far) intersections; getting these far intersections, conversely, will dilate the near intersection. The expected URDF retains

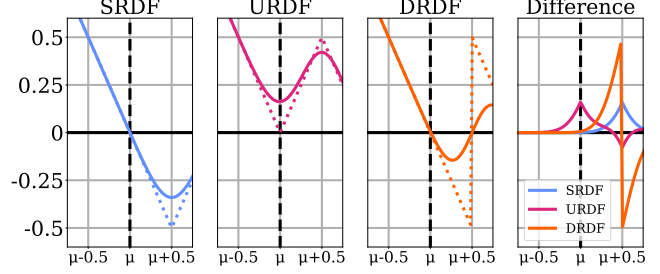


Figure 4. Suppose the surface’s location is normally distributed with mean μ at its true location and $\sigma=0.2$, and the next surface 1 is unit away. We plot the expected (solid) and true (dashed) distance functions for the SRDF, URDF, and DRDF and their difference (expected - true). The SRDF and DRDF closely match the true distance near the surface; the URDF does not.

the zero-crossing of the derivative, but the discontinuity is blunted and our empirical results suggest that finding the zero-crossing is less effective than other schemes. Similar effects hamper proximity based occupancy: the optimal output at z is the chance a surface is within r , which squashes the network output in an uncertainty-dependent fashion.

The DRDF is more stable under uncertainty. Finding a zero-crossing requires no tuning, and the zero-crossing at the intersection is preserved except when σ is large (e.g., $\sigma=\frac{n}{3}$), at which point other functions have also broken down. This is because its uncertainty-driven distortions occur halfway to the other intersection. The only nuance is a second zero-crossing after the intersection, which can be ignored by filtering based on the direction of the crossing.

Limitations. We briefly discuss some limitations of our analysis, with full details in the supplement. *LI-vs-MSE:* our results are for $E_S[d(z; s)]$ (which optimizes the MSE) rather than the median (which optimizes the L1 loss); empirically, we find these values to be usually nearly identical, due to the symmetry of our noise. *Rays-vs-Scenes:* Our analysis focuses on rays. Our analysis of UDRFs directly extends to a UDF to a plane under isotropic Gaussian noise, which has the same form as the URDF but with point-plane distance. In general, the expected UDF with non-trivial noise is non-zero since it is a convex combination of 0 and positive values. *Training Effects:* Our analysis describes the optimal behavior of the network; while our networks may not achieve this, we find good qualitative agreement.

3.4. Implementation Details

We now describe the implementation of our network. We use this network to estimate a variety of distance functions, and so our presentation is generic until the decoding step.

Training. Given samples $\{\mathbf{x}_i, I_i, d_i\}_{i=1}^n$ consisting of 3D points, images, and target distance functions respectively, we train our network to minimize the L1 loss, $\sum_{i=1}^n |d_i - h_\theta(v(\mathbf{x}_i, b_\theta(I_i)))|$, where the predictions are in log-space

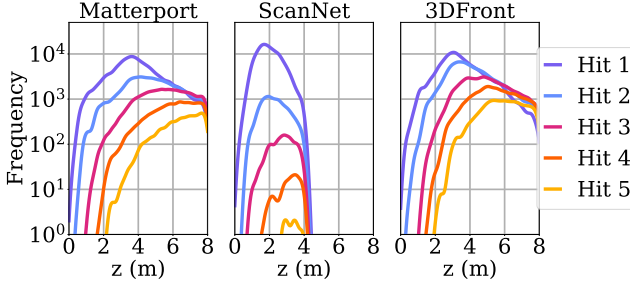


Figure 5. Ray Hit count distribution. We compare the distribution over surface hit locations for first 4 hits over 1M rays and observe that ScanNet has $\leq 1\%$ rays as compared to Matterport and 3DFront which have $\geq 25\%$ rays with more than 2 hits

truncated at 1m following other methods that predict TS-DFs [11, 47]. We optimize using AdamW [29, 33] using a learning rate of 10^{-4} . We sample points \mathbf{x}_i for each scene two ways: for each intersection at l , we sample 512 points from $\mathcal{N}(l, 0.1)$; for each ray we sample 512 points uniformly from 0 to a maximum prediction depth. We do this for 20 intersections and 20 rays per scene in a batch. We train with a batch size of 10 for 250K iterations and freeze batch norm layers after $\frac{1}{4}$ th of the iterations.

Inference. At inference time, we extract backbone features at a regular $N \times N$ grid ($N=128$) in one forward pass of b . For each grid point, we predict the distance function for $K = 128$ points linearly spaced on each ray from 0 to a maximum depth. This entails making $N^2 K$ predictions with the regression head, which is parallelizable, yielding a frustum-shaped volume of locations with predictions. Once a distance volume is predicted, methods vary in how they decode the distances to surfaces. The DRDF requires finding positive zero-crossings; we explain others in §4.1.

4. Experiments

We evaluate DRDF on real images of scenes and compare to alternate choices of distance functions and formulations of the scene prediction problem such as Layered Depth Images[44]. We also try extensive variants of decoding schemes for our baseline methods. Our experiments evaluate both the methods ability to predict the visible and occluded parts of the scene using standard metrics and new metric that evaluates along rays.

Metrics. We use three metrics. No one metric properly quantifies reconstruction as each captures a different aspect of the task [49]. The first is scene chamfer errors at multiple thresholds. The others are accuracy/completeness [43] and their harmonic mean, F1-score [49], for scenes and rays (focusing on occluded points).

Chamfer L1. We compute Symmetric Chamfer L1 error for each scene with 30K points sampled from the ground truth and the prediction. We plot the fraction of scenes with Symmetric Chamfer L1 errors that are less than t for $t \in [0, 1]\text{m}$.

This is more informative than just the mean across the dataset and compares performance over the curve.

Scene (Acc/Cmp/F1). Like [43, 49], we report accuracy/Acc (% of predicted points within t of the ground-truth), completeness/Cmp (% of ground-truth points within t of the prediction), and their harmonic mean, F1-score. This gives a summary of overall scene-level accuracy.

Rays (Acc/Cmp/F1), Occluded Points. We additionally evaluate each ray independently, measuring Acc/Cmp/F1 on each ray and reporting the mean. In the paper, we report results for occluded points (defined as all surfaces past the first for both ground-truth and predicted). The supplement contains full results. Evaluating each ray independently applies a more stringent test for occluded surfaces compared to scenes: with scene-level evaluation on a high resolution image, a prediction can miss a hidden surface (e.g., the 2nd surface) on every other pixel since the missing predictions will be covered for by hidden surfaces in adjacent rays. Ray-based evaluation, however, requires each pixel to have all hidden surfaces present to receive full credit.

Datasets. We desire three key properties in datasets: the images should be real to prevent the abuse of rendering artifacts; the mesh should be a real capture since mimicking capture holes is itself a research problem; and the data ought to have lots of occluded geometry. Our primary dataset is Matterport3D [5], which satisfies all properties. We also evaluate on 3DFront [17] and ScanNet [10]. While 3DFront does not have capture holes, cutting it with a view frustum creates holes. ScanNet [10] is a popular dataset in 3D reconstruction, but has far less occluded geometry compared to the other datasets. A full description of the datasets appears in the supplement.

Matterport3D [5]. We use the *raw images* captured with the Matterport camera. We split the 90 scenes into train/val/test (60/15/15) and remove images that are too close to the mesh ($\geq 60\%$ of image within 1m) or are $> 20^\circ$ away from level. We then sample 13K/1K/1K images for train/val/test set.

3DFront [17]. This is a synthetic dataset of houses created by artists with underlying hole-free 3D geometry. We collect 4K scenes from 3DFront [17] after removing scenes with missing annotations. We select 20 camera poses and filter for bad camera poses similar in Matterport3D [5]. Our train set has 3K scenes with approximately 47K images. Our val and test sets have 500 scenes with 1K images each.

ScanNet [10]. We use splits from [10] (1045/156/312 train/val/test) and randomly select 5 images per scene for train set, and 10 images per scene for val/test set. We then sample to a set of 33K/1K/1K images per train/val/test.

Scene Statistics. To give a sense of scene statistics, we plot the frequency of the locations of the first 5 hits for each dataset (computed on 1M rays each) in Figure 5. 99% of ScanNet rays have 1 or 2 hits, while $\geq 24\%$ of Matterport3D [5] and 3DFront [17] rays have more than 2 hits.

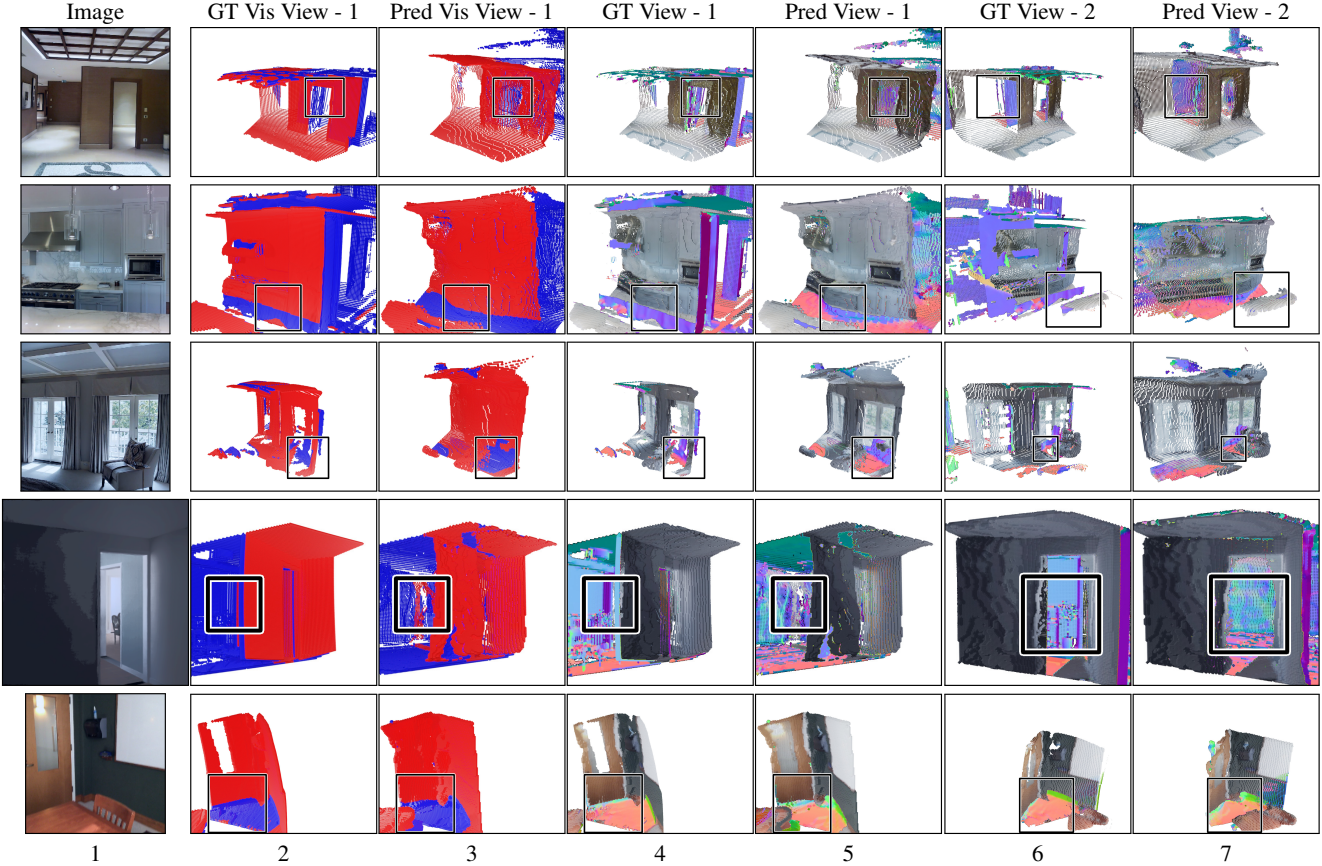


Figure 6. Novel views from DRDF We render outputs of our method and the ground-truth from new viewpoints with $\geq 45^\circ$ view change. Columns 2 & 3 show new views where **visible points are red** and **occluded points are blue**. In other columns, we color the visible regions with the image and occluded regions with computed surface normals (FLAG scheme from camera inside a cube). DRDF recovers occluded regions, such as a room behind the door (row 1 & 4), a hidden floor behind the kitchen counter (row 2), and a wall and floor behind the chair/couch (row 3 & 5). Rows 1-3 are Matterport3D [5]; Row4 is 3DFront [17]; Row 5 is ScanNet [10].

4.1. Baselines

We compare against baselines to test our contributions. For fair comparison, all approaches use the same ResNet-34 [22] backbone and extract features from multiple layers via bilinear interpolation [56]. Thus, different distance functions are trained identically by replacing the target distance. Each method’s description consists of two parts: a prediction space parameterization and a decoding strategy to convert the inferred distances to surfaces.

Picking decoding strategies. Most baselines predict a distance function rather than a set of intersections and thus need a decoding strategy to convert distances to a set of surface locations. Some baselines have trivial strategies: LDI directly outputs intersections; SAL and DRDF use zero-crossings and have no parameters. However, UDF, URDF, and ORF are sensitive to decoding strategy. We tried multiple strategies for each based on past work and theoretical analysis of their behavior and report the best strategy (measured with Scene F1 on Matterport3D [5]) as well as alter-

nates. When decoding strategies have detection parameters, we tune to ensure similar completeness to our method. Accuracy and completeness trade-off, and having one roughly fixed ensures that methods are being compared at similar points on the operating curve, making F1 score meaningful.

Layered Depth Images (LDI). To test the value of framing the problem as implicit function prediction, we train a method to predict a k -channel depthmap where the i^{th} output is trained to predict the i^{th} intersection along the ray through the pixel. We use a L1 loss per pixel and intersection. We set $k = 4$, the same number of intersections the proposed approach uses.

Decoding. The LDI directly predicts surface locations.

Layered Depth Images with Confidence (LDI + Conf.). We augment the the LDI baseline with k additional channels that represent the likelihood the i^{th} intersection exists. These added channels are trained with binary cross-entropy.

Decoding. For each pixel, we accept or ignore each layer based on the whether the predicted probability exceeds 0.5.

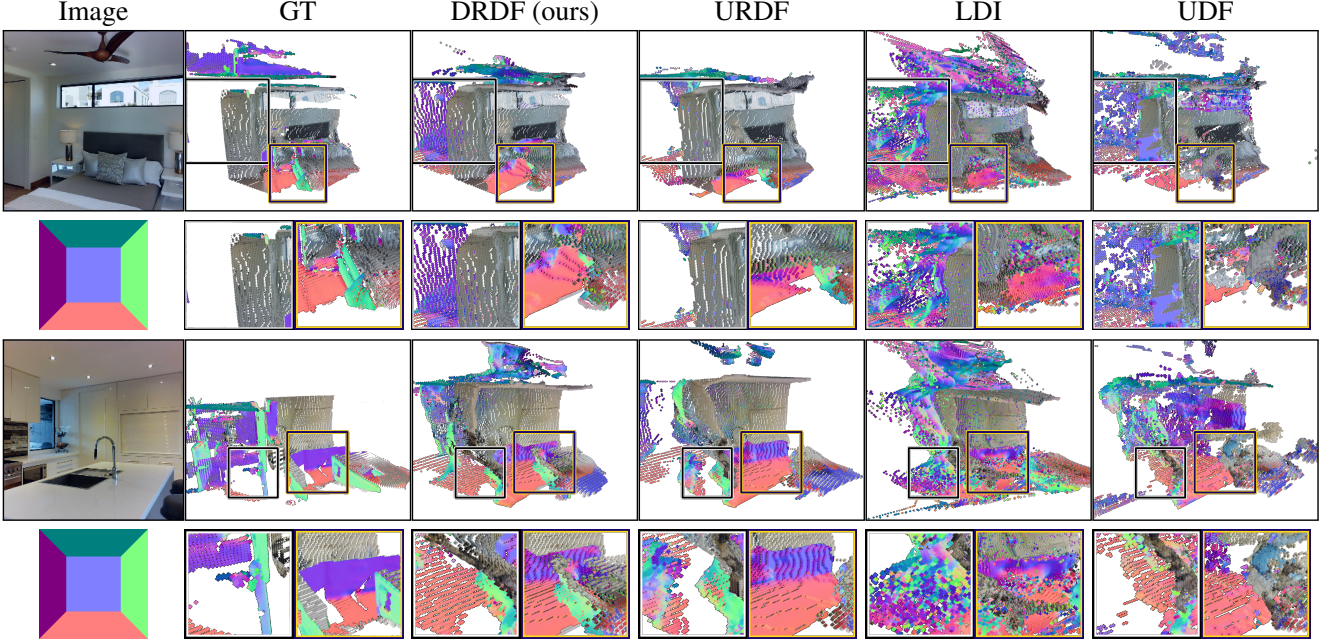


Figure 7. Qualitative Comparison with Baselines We render the generated 3D outputs in a new view (rotate left ←). We show two crops on the next row for better visual comparison. Visible regions are colored using the image and occluded regions are colored with surface normals (color scheme with a camera inside the cube). DRDF produces higher quality results compared to LDI and UDF (row 1, 2, more consistency, smoother surface, no blobs). In row 1 (crop 2), URDF misses parts of floor; in row 2 (crop 2), URDF misses the green colored side of the kitchen counter. See supp. for more results.

Unsigned Distance Function (UDF) [8]. To test the value of predicting distances on rays, we learn to predict the UDF to the scene rather than the ray.

Decoding. We use `scipy.argrelextrema` [53] to find local extrema. We find local minimas of the distance function within a 1m window along the ray. We found this works better than absolute thresholding (by 14.7 on F1). Sphere tracing and gradient-based optimization as proposed by [8] performs substantially worse (25.7 on F1), likely since it assumes the predicted UDF behaves similar to a GT UDF.

Unsigned Ray Distance Function (URDF). For direct comparison with ray-vs-scene held constant, we compare with the URDF.

Decoding. Decoding a URDF is challenging. We perform non-maximum suppression on the thresholded data by finding connected components of the ray that have predicted distance below a tuned-constant τ , and keep the first prediction as the surface location. We found this to outperform: thresholding (by 5.3 on F1); finding zero-crossings of the numerical gradient (by 11 on F1); and using sphere tracing and gradient-based optimization as in [8] (by 6.6 on F1).

Ray Sign-Agnostic Learning Loss (SAL) [1]. Traditional SDF learning is impossible due to the non-watertightness of the data and so we use the sign agnostic approach proposed by [1]. We initialize our architecture with the SAL initialization and train with the SAL loss. The SAL approach

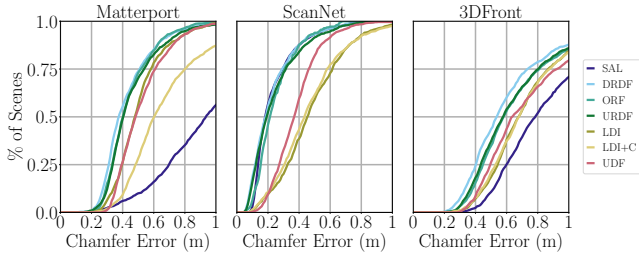


Figure 8. Chamfer L1 distances. We plot % of scenes on Y-axis as function of symmetric Chamfer L1 error below a threshold t on X-axis. On Matterport and 3DFront datasets DRDF is better and comparable to the best alternate method on ScanNet.

assumes that while the data may not be watertight due to noisy capture, the underlying model is watertight. In this case, rays start and end *outside* objects (and thus the number of hits along each ray is even). This is not necessarily the case on Matterport3D [5] and 3DFront [17].

Decoding. Following [1], we find surfaces as zero-crossings of the predicted distance function along the ray.

Ray Occupancy (ORF). Traditional interior/exterior occupancy is impossible on non-watertight data, but one can predict whether a point is within r of a surface as a classification problem. This tests the value of predicting distances, and not just occupancy. We tried several values of r ([0.1, 0.25, 0.5, 1]m) and report the best-performing version.

Table 1. Scene Acc/Comp/F1Score. Thresholds: 0.5m (MP3D [5], 3DFront [17]), 0.2m (ScanNet [10]). **Bold is best**, underline is 2nd best per column. DRDF is best in F1 and accuracy, and always comparable to the best in completeness.

Method	MP3D [5]			3DFront [17]			ScanNet [10]		
	Acc	Cmp	F1	Acc	Cmp	F1	Acc	Cmp	F1
LDI	66.2	72.4	67.4	68.6	46.5	52.7	19.3	28.6	21.5
LDI +C	64.8	55.1	57.7	70.8	45.1	52.4	19.9	32.0	23.3
SAL [1]	66.1	25.5	34.3	80.7	28.5	39.5	51.2	70.0	57.7
UDF	58.7	76.0	64.7	70.1	<u>51.9</u>	57.4	44.4	62.6	50.8
ORF	73.4	69.4	<u>69.6</u>	<u>86.4</u>	48.1	<u>59.6</u>	51.5	58.5	53.7
URDF	74.5	67.1	68.7	85.0	47.7	58.7	<u>61.0</u>	57.8	<u>58.2</u>
DRDF (ours)	75.4	72.0	71.9	87.3	52.6	63.4	62.0	<u>62.7</u>	60.9

Decoding. Each surface in the prediction is, in theory surrounded by two crossings each with probability 0.5 that are equidistant from the surface: an onset/rising crossing and offset/falling crossing. Finding 0.5-crossings leads to doubled predictions. Instead, we consider all adjacent and nearby pairs of offsets and onsets, and average them; unpaired crossings are kept on their own. We found this outperformed keeping just a single crossings (by 4.7 on F1).

4.2. Results

Qualitative Results. Qualitative results of our method appear throughout the paper (by itself in Fig. 6 and compared to baselines in Fig. 7). Our approach is often able to generate parts of the occluded scene, such as a room behind a door, cabinets and floor behind kitchen counters, and occluded regions behind furniture. Sometimes the method completes holes in the ground-truth that are due to scanning error. On the other hand we see our method sometimes fails to characterize the missing parts as detailed occluded 3D.

Compared to baselines, our approach generally does qualitatively better. LDI and UDF often have floating blobs or extruded regions, due to either predicting too many layers (LDI) or having a distance function that is challenging to manage (UDF). URDF produces qualitatively better results, but often misses points, especially in occluded regions.

Quantitative Results. These results are borne out in the quantitative results. We report the Chamfer plot in Figure 8, the scene distance metrics in Tab. 1 and occluded surfaces metrics along rays in Tab. 2. DRDF consistently does at least as well, or substantially better than the baselines on Chamfer. In general, DRDF does substantially better than all baselines. In a few situations, a baseline outperforms DRDF in completeness at the cost of substantially worse accuracy. However, no one baseline is competitive with DRDF *across* datasets: SAL works well on ScanNet [10] and LDI works well on MP3D [5].

LDI performs worse than DRDF because it cannot vary its number of intersections; simply adding a second stack

Table 2. Ray Acc/Comp/F1Score on Occluded Points. Thresholds: 0.5m (MP3D [5], 3DFront [17]), 0.2m (ScanNet [10]). DRDF is best on F1 and Acc, and is occasionally 2nd best on Cmp. Gains on occluded points are even larger than the full scene.

Method	MP3D [5]			3DFront [17]			ScanNet [10]		
	Acc	Cmp	F1	Acc	Cmp	F1	Acc	Cmp	F1
LDI	13.9	42.8	19.3	17.8	35.8	22.2	0.5	9.0	2.4
LDI +C	18.7	21.7	19.3	17.7	22.6	19.9	1.1	2.4	3.5
SAL [1]	5.5	0.5	3.5	24.1	4.3	11.4	2.4	38.7	5.6
UDF	15.5	23.0	16.6	29.3	21.3	23.4	1.8	7.8	5.5
ORF	<u>26.2</u>	20.5	<u>21.6</u>	53.2	22.0	<u>31.0</u>	6.6	12.3	11.4
URDF	24.9	20.6	20.7	47.7	23.3	30.2	<u>8.4</u>	11.6	13.8
DRDF (ours)	28.4	30.0	27.3	54.6	56.0	52.6	9.0	20.4	16.0

of outputs (LDI + C.) is insufficient. We hypothesize this is because DRDF can learn *where* things tend to be, while LDI-based methods also have to learn the order in which things occur (e.g., is the floor 2nd intersection or the 3rd intersection at this pixel?). SAL performs competitively on ScanNet, likely because of the relatively limited variability in numbers of intersections per ray; when tested on Matterport3D and 3DFront, its performance drops substantially.

The most straightforward way to learn on non-watertight data is to predict unsigned scene distances [8] which has been shown to work with memorizing 3D scenes. However, predicting it from a single image is a different problem entirely, and scene distances require integration of information over large areas. This leads to poor performance. Predicting distances on rays can alleviate this challenge, but recovering intersections remains hard even with multiple decoding strategies. Hence, DRDF outperforms URDF on scene metrics and even more so on occluded points in Tab. 2. Similarly ORF too requires decoding strategies and is sensitive to training parameter choices. In contrast, by accounting for the uncertainty in surface location, DRDF requires a simple decoding strategy and outperforms the other methods.

Conclusions. We have introduced a method for predicting full 3D from a single RGB image with implicit functions. Our contribution is a new distance-like function, the DRDF, and show it has more desirable theoretical properties under uncertainty compared to standard unsigned distance function. When we use DRDF in an implicit function method and train on 3D scan datasets, we show it obtains substantially better performance compared to existing approaches.

Our approach advances the state of the art in 3D from a single image, which can in turn be used for tasks as varied as content creation to AR/VR to autonomous systems. Many have positive applications, but some do not. Moreover, much of our data does not reflect most peoples’ reality – MP3D, for instance, has many lavish houses – and so this may widen technological gaps. On the other hand, by handling non-watertight scans, our system may enable learning from scans collected by ordinary people rather than experts.

References

- [1] Matan Atzmon and Yaron Lipman. Sal: Sign agnostic learning of shapes from raw data. In *Proceedings of the IEEE/CVF Conference on Computer Vision and Pattern Recognition*, pages 2565–2574, 2020. [1](#), [2](#), [7](#), [8](#)
- [2] Matan Atzmon and Yaron Lipman. Sal++: Sign agnostic learning with derivatives. *arXiv preprint arXiv:2006.05400*, 2020. [1](#), [2](#)
- [3] Gwangbin Bae, Ignas Budvytis, and Roberto Cipolla. Estimating and exploiting the aleatoric uncertainty in surface normal estimation. In *Proceedings of the IEEE/CVF International Conference on Computer Vision*, pages 13137–13146, 2021. [2](#)
- [4] Harry Barrow, J Tenenbaum, A Hanson, and E Riseman. Recovering intrinsic scene characteristics. *Comput. Vis. Syst.*, 2(3-26):2, 1978. [2](#)
- [5] Angel Chang, Angela Dai, Thomas Funkhouser, Maciej Halber, Matthias Niessner, Manolis Savva, Shuran Song, Andy Zeng, and Yinda Zhang. Matterport3d: Learning from rgb-d data in indoor environments. *arXiv preprint arXiv:1709.06158*, 2017. [1](#), [2](#), [3](#), [5](#), [6](#), [7](#), [8](#)
- [6] Angel X Chang, Thomas Funkhouser, Leonidas Guibas, Pat Hanrahan, Qixing Huang, Zimo Li, Silvio Savarese, Manolis Savva, Shuran Song, Hao Su, et al. Shapenet: An information-rich 3d model repository. *arXiv preprint arXiv:1512.03012*, 2015. [1](#), [2](#)
- [7] Zhiqin Chen and Hao Zhang. Learning implicit fields for generative shape modeling. In *Proceedings of the IEEE/CVF Conference on Computer Vision and Pattern Recognition*, pages 5939–5948, 2019. [1](#), [2](#)
- [8] Julian Chibane, Aymen Mir, and Gerard Pons-Moll. Neural unsigned distance fields for implicit function learning. In *Advances in Neural Information Processing Systems (NeurIPS)*, December 2020. [1](#), [2](#), [7](#), [8](#)
- [9] Christopher B Choy, Danfei Xu, JunYoung Gwak, Kevin Chen, and Silvio Savarese. 3d-r2n2: A unified approach for single and multi-view 3d object reconstruction. In *European conference on computer vision*, pages 628–644. Springer, 2016. [1](#), [2](#)
- [10] Angela Dai, Angel X Chang, Manolis Savva, Maciej Halber, Thomas Funkhouser, and Matthias Nießner. Scannet: Richly-annotated 3d reconstructions of indoor scenes. In *Proceedings of the IEEE Conference on Computer Vision and Pattern Recognition*, pages 5828–5839, 2017. [1](#), [2](#), [5](#), [6](#), [8](#)
- [11] Angela Dai, Christian Diller, and Matthias Nießner. Sg-nn: Sparse generative neural networks for self-supervised scene completion of rgb-d scans. In *Proceedings of the IEEE/CVF Conference on Computer Vision and Pattern Recognition*, pages 849–858, 2020. [5](#)
- [12] Luca Del Pero, Joshua Bowdish, Bonnie Kermgard, Emily Hartley, and Kobus Barnard. Understanding bayesian rooms using composite 3d object models. In *Proceedings of the IEEE Conference on Computer Vision and Pattern Recognition (CVPR)*, June 2013. [2](#)
- [13] Helisa Dhamo, Nassir Navab, and Federico Tombari. Object-driven multi-layer scene decomposition from a single image. In *Proceedings of the IEEE/CVF International Conference on Computer Vision*, pages 5369–5378, 2019. [2](#)
- [14] Haoqiang Fan, Hao Su, and Leonidas J Guibas. A point set generation network for 3d object reconstruction from a single image. In *Proceedings of the IEEE conference on computer vision and pattern recognition*, pages 605–613, 2017. [2](#)
- [15] Sanja Fidler, Sven Dickinson, and Raquel Urtasun. 3d object detection and viewpoint estimation with a deformable 3d cuboid model. In *Advances in neural information processing systems*, pages 611–619, 2012. [2](#)
- [16] David F Fouhey, Abhinav Gupta, and Martial Hebert. Data-driven 3d primitives for single image understanding. In *Proceedings of the IEEE International Conference on Computer Vision*, pages 3392–3399, 2013. [2](#)
- [17] Huan Fu, Bowen Cai, Lin Gao, Lingxiao Zhang, Cao Li, Qixun Zeng, Chengyue Sun, Yiyun Fei, Yu Zheng, Ying Li, Yi Liu, Peng Liu, Lin Ma, Le Weng, Xiaohang Hu, Xin Ma, Qian Qian, Rongfei Jia, Binqiang Zhao, and Hao Zhang. 3d-front: 3d furnished rooms with layouts and semantics. *arXiv preprint arXiv:2011.09127*, 2020. [2](#), [5](#), [6](#), [7](#), [8](#)
- [18] Rohit Girdhar, David F Fouhey, Mikel Rodriguez, and Abhinav Gupta. Learning a predictable and generative vector representation for objects. In *European Conference on Computer Vision*, pages 484–499. Springer, 2016. [1](#), [2](#)
- [19] Georgia Gkioxari, Jitendra Malik, and Justin Johnson. Mesh r-cnn. In *Proceedings of the IEEE International Conference on Computer Vision*, pages 9785–9795, 2019. [2](#)
- [20] Thibault Groueix, Matthew Fisher, Vladimir G Kim, Bryan C Russell, and Mathieu Aubry. A papier-mâché approach to learning 3d surface generation. In *Proceedings of the IEEE conference on computer vision and pattern recognition*, pages 216–224, 2018. [2](#)
- [21] Christian Häne, Shubham Tulsiani, and Jitendra Malik. Hierarchical surface prediction for 3d object reconstruction. In *2017 International Conference on 3D Vision (3DV)*, pages 412–420. IEEE, 2017. [2](#)
- [22] Kaiming He, Xiangyu Zhang, Shaoqing Ren, and Jian Sun. Deep residual learning for image recognition. In *Proceedings of the IEEE conference on computer vision and pattern recognition*, pages 770–778, 2016. [6](#)
- [23] Varsha Hedau, Derek Hoiem, and David Forsyth. Recovering the spatial layout of cluttered rooms. In *2009 IEEE 12th international conference on computer vision*, pages 1849–1856. IEEE, 2009. [2](#)
- [24] Derek Hoiem, Alexei A Efros, and Martial Hebert. Geometric context from a single image. In *Tenth IEEE International Conference on Computer Vision (ICCV'05) Volume 1*, volume 1, pages 654–661. IEEE, 2005. [2](#)
- [25] Theerasit Issaranon, Chuhang Zou, and David Forsyth. Counterfactual depth from a single rgb image. In *Proceedings of the IEEE/CVF International Conference on Computer Vision Workshops*, pages 0–0, 2019. [2](#)
- [26] Hamid Izadinia, Qi Shan, and Steven M Seitz. Im2cad. In *Proceedings of the IEEE Conference on Computer Vision and Pattern Recognition*, pages 5134–5143, 2017. [2](#)
- [27] Ziyu Jiang, Buyu Liu, Samuel Schulter, Zhangyang Wang, and Manmohan Chandraker. Peek-a-boo: Occlusion reasoning in indoor scenes with plane representations. In *Proceedings of the IEEE/CVF Conference on Computer Vision and Pattern Recognition*, pages 113–121, 2020. [2](#)

- [28] Alex Kendall and Yarin Gal. What uncertainties do we need in bayesian deep learning for computer vision? In *Proceedings of the 31st International Conference on Neural Information Processing Systems*, pages 5580–5590, 2017. 2
- [29] Diederik P Kingma and Jimmy Ba. Adam: A method for stochastic optimization. *arXiv preprint arXiv:1412.6980*, 2014. 5
- [30] Nilesh Kulkarni, Ishan Misra, Shubham Tulsiani, and Abhinav Gupta. 3d-relnet: Joint object and relational network for 3d prediction. In *Proceedings of the IEEE International Conference on Computer Vision*, pages 2212–2221, 2019. 2
- [31] Lin Li, Salman Khan, and Nick Barnes. Silhouette-assisted 3d object instance reconstruction from a cluttered scene. In *ICCV Workshops*, 2019. 2
- [32] Chen-Hsuan Lin, Chen Kong, and Simon Lucey. Learning efficient point cloud generation for dense 3d object reconstruction. *arXiv preprint arXiv:1706.07036*, 2017. 2
- [33] Ilya Loshchilov and Frank Hutter. Decoupled weight decay regularization. *arXiv preprint arXiv:1711.05101*, 2017. 5
- [34] Ricardo Martin-Brualla, Noha Radwan, Mehdi SM Sajjadi, Jonathan T Barron, Alexey Dosovitskiy, and Daniel Duckworth. Nerf in the wild: Neural radiance fields for unconstrained photo collections. *arXiv preprint arXiv:2008.02268*, 2020. 2
- [35] Lars Mescheder, Michael Oechsle, Michael Niemeyer, Sebastian Nowozin, and Andreas Geiger. Occupancy networks: Learning 3d reconstruction in function space. In *Proceedings of the IEEE Conference on Computer Vision and Pattern Recognition*, pages 4460–4470, 2019. 1, 2
- [36] Ben Mildenhall, Pratul P Srinivasan, Matthew Tancik, Jonathan T Barron, Ravi Ramamoorthi, and Ren Ng. Nerf: Representing scenes as neural radiance fields for view synthesis. *arXiv preprint arXiv:2003.08934*, 2020. 2, 3
- [37] Yinyu Nie, Xiaoguang Han, Shihui Guo, Yujian Zheng, Jian Chang, and Jian Jun Zhang. Total3dunderstanding: Joint layout, object pose and mesh reconstruction for indoor scenes from a single image. In *Proceedings of the IEEE/CVF Conference on Computer Vision and Pattern Recognition*, pages 55–64, 2020. 2
- [38] Jeong Joon Park, Peter Florence, Julian Straub, Richard Newcombe, and Steven Lovegrove. Deepsdf: Learning continuous signed distance functions for shape representation. In *Proceedings of the IEEE Conference on Computer Vision and Pattern Recognition*, pages 165–174, 2019. 1, 2
- [39] Matteo Poggi, Filippo Aleotti, Fabio Tosi, and Stefano Mattoccia. On the uncertainty of self-supervised monocular depth estimation. In *Proceedings of the IEEE/CVF Conference on Computer Vision and Pattern Recognition*, pages 3227–3237, 2020. 2
- [40] Shunsuke Saito, Zeng Huang, Ryota Natsume, Shigeo Morishima, Angjoo Kanazawa, and Hao Li. Pifu: Pixel-aligned implicit function for high-resolution clothed human digitization. In *Proceedings of the IEEE International Conference on Computer Vision*, pages 2304–2314, 2019. 1, 2
- [41] Shunsuke Saito, Tomas Simon, Jason Saragih, and Hanbyul Joo. Pifuhd: Multi-level pixel-aligned implicit function for high-resolution 3d human digitization. In *Proceedings of the IEEE/CVF Conference on Computer Vision and Pattern Recognition*, pages 84–93, 2020. 2
- [42] Ashutosh Saxena, Min Sun, and Andrew Y Ng. Make3d: Learning 3d scene structure from a single still image. *IEEE transactions on pattern analysis and machine intelligence*, 31(5):824–840, 2008. 2
- [43] Steven M Seitz, Brian Curless, James Diebel, Daniel Scharstein, and Richard Szeliski. A comparison and evaluation of multi-view stereo reconstruction algorithms. In *2006 IEEE computer society conference on computer vision and pattern recognition (CVPR’06)*, volume 1, pages 519–528. IEEE, 2006. 5
- [44] Jonathan Shade, Steven Gortler, Li-wei He, and Richard Szeliski. Layered depth images. In *Proceedings of the 25th annual conference on Computer graphics and interactive techniques*, pages 231–242, 1998. 2, 5
- [45] Vincent Sitzmann, Julien Martel, Alexander Bergman, David Lindell, and Gordon Wetzstein. Implicit neural representations with periodic activation functions. *Advances in Neural Information Processing Systems*, 33, 2020. 1, 2
- [46] Shuran Song, Fisher Yu, Andy Zeng, Angel X Chang, Manolis Savva, and Thomas Funkhouser. Semantic scene completion from a single depth image. In *Proceedings of the IEEE Conference on Computer Vision and Pattern Recognition*, pages 1746–1754, 2017. 2
- [47] Jiaming Sun, Yiming Xie, Linghao Chen, Xiaowei Zhou, and Hujun Bao. Neuralrecon: Real-time coherent 3d reconstruction from monocular video. In *Proceedings of the IEEE/CVF Conference on Computer Vision and Pattern Recognition*, pages 15598–15607, 2021. 5
- [48] Xingyuan Sun, Jiajun Wu, Xiuming Zhang, Zhoutong Zhang, Chengkai Zhang, Tianfan Xue, Joshua B Tenenbaum, and William T Freeman. Pix3d: Dataset and methods for single-image 3d shape modeling. In *Proceedings of the IEEE Conference on Computer Vision and Pattern Recognition*, pages 2974–2983, 2018. 2
- [49] Maxim Tatarchenko, Stephan R Richter, René Ranftl, Zhuwen Li, Vladlen Koltun, and Thomas Brox. What do single-view 3d reconstruction networks learn? In *Proceedings of the IEEE Conference on Computer Vision and Pattern Recognition*, pages 3405–3414, 2019. 5
- [50] Shubham Tulsiani, Saurabh Gupta, David F Fouhey, Alexei A Efros, and Jitendra Malik. Factoring shape, pose, and layout from the 2d image of a 3d scene. In *Proceedings of the IEEE Conference on Computer Vision and Pattern Recognition*, pages 302–310, 2018. 2
- [51] Shubham Tulsiani, Hao Su, Leonidas J Guibas, Alexei A Efros, and Jitendra Malik. Learning shape abstractions by assembling volumetric primitives. In *Proceedings of the IEEE Conference on Computer Vision and Pattern Recognition*, pages 2635–2643, 2017. 2
- [52] Shubham Tulsiani, Richard Tucker, and Noah Snavely. Layer-structured 3d scene inference via view synthesis. In *ECCV*, 2018. 2
- [53] Pauli Virtanen, Ralf Gommers, Travis E Oliphant, Matt Haberland, Tyler Reddy, David Cournapeau, Evgeni Burovski, Pearu Peterson, Warren Weckesser, Jonathan Bright, Stéfan J. van der Walt, Matthew Brett, Joshua Wilson, K. Jarrod Millman, Nikolay Mayorov, Andrew R. J. Nelson, Eric Jones, Robert Kern, Eric Larson, C J Carey, İlhan Polat, Yu Feng, Eric W. Moore, Jake VanderPlas, De-

- nis Laxalde, Josef Perktold, Robert Cimrman, Ian Henriksen, E. A. Quintero, Charles R. Harris, Anne M. Archibald, Antônio H. Ribeiro, Fabian Pedregosa, Paul van Mulbregt, and SciPy 1.0 Contributors. SciPy 1.0: Fundamental Algorithms for Scientific Computing in Python. *Nature Methods*, 17:261–272, 2020. 7
- [54] Nanyang Wang, Yinda Zhang, Zhuwen Li, Yanwei Fu, Wei Liu, and Yu-Gang Jiang. Pixel2mesh: Generating 3d mesh models from single rgb images. In *ECCV*, 2018. 1
- [55] Qiangeng Xu, Weiyue Wang, Duygu Ceylan, Radomir Mech, and Ulrich Neumann. Disn: Deep implicit surface network for high-quality single-view 3d reconstruction. In *Advances in Neural Information Processing Systems*, pages 492–502, 2019. 2
- [56] Alex Yu, Vickie Ye, Matthew Tancik, and Angjoo Kanazawa. pixelNeRF: Neural radiance fields from one or few images. In *CVPR*, 2021. 2, 6
- [57] Kai Zhang, Gernot Riegler, Noah Snavely, and Vladlen Koltun. Nerf++: Analyzing and improving neural radiance fields. *arXiv preprint arXiv:2010.07492*, 2020. 2

What's Behind the Couch? Directed Ray Distance Functions (DRDF) for 3D Scene Reconstruction

Nilesh Kulkarni

Justin Johnson

David F. Fouhey

University of Michigan

{nileshk, justincj, fouhey}@umich.edu

Contents

1. Overview	1
2. Experiments	1
2.1. Additional Evaluation for Baselines	1
2.2. Effect of different Decodings	2
3. Dataset Details	3
4. Video Results & Interactive Demo	3
4.1. Video Results	3
4.2. Interactive Demo	3
5. Distance Functions Under Uncertainty	4
5.1. Signed Ray Distance Function (SRDF)	5
5.2. Unsigned Ray Distance Function (URDF)	5
5.3. (Proximity) Occupancy Ray Function (ORF)	5
5.4. Directed Ray Distance Function	6
5.5. Median vs Expectation	7
5.6. Unsigned Distance Function to A Plane in 3D	8
6. Qualitative Results	10
7. Derivations	17
7.1. Signed Ray Distance Function	17
7.2. Unsigned Ray Distance Function	17
7.3. Occupancy Ray Function	18
7.4. Directed Ray Distance Function	18
7.5. Planes	19

1. Overview

We present additional details such as qualitative results and experiments in the supplemental materials. Our supplemental is divided into three kinds of materials.

Supplemental PDF. Our PDF consists of details of experiments for scene and ray based evaluation. This is discussed under §2.1 along with new evaluations promised in the main

paper. In §2.2 we provide full experiment evaluation of different decoding strategies of baselines. §3 discusses additional details for datasets. In §4.1 and §4.2 we have details on video results and interactive demo respectively. We then in §5 discuss the detail behavior of various distance functions under uncertainty and provide uncertainty plots. We follow it up by additional qualitative results on all the three datasets from randomly sampled images on the test set in §6. In §7 we derive the results mathematically to showcase the analysis technique for other distance functions.

Video Results. We provide 3D visualizations as video from our model and we recommend watching these. Details under §4.1

Interactive Results. We present interactive demo of our model (DRDF) and the GT on images sampled on Matterport3D [2]. Instructions to run the demo in §4.2

2. Experiments

2.1. Additional Evaluation for Baselines

In the main paper we presented results from Tab. 1 (scene based evaluation) and Tab. 2 (ray based evaluation on occluded points). Additionally we also present ray based evaluation on all intersections/points along the ray in Tab. 3. We present results on all the three datasets Matterport, 3DFront, and ScanNet like in the main paper. Now for the sake of completeness we revisit the metrics again.

Scene (Acc/Cmp/F1). Like [6, 7], we report accuracy/Acc (% of predicted points within t of the ground-truth), completeness/Cmp (% of ground-truth points within t of the prediction), and their harmonic mean, F1-score. This gives a summary of overall scene-level accuracy. Results are reported in Tab. 1 as presented in the main paper.

Rays (Acc/Cmp/F1), Occluded Points. We additionally evaluate each ray independently, measuring Acc/Cmp/F1 on each ray and reporting the mean. Occluded points are defined as all surfaces past the first for both ground-truth and predicted. Evaluating each ray independently applies a more stringent test for occluded surfaces compared to

Table 1: (From Main Paper) Scene Acc/Comp/F1Score. Thresholds: 0.5m (MP3D [2], 3DFront [5]), 0.2m (ScanNet [4]). **Bold is best**, underline is 2nd best per column. DRDF is best in F1 and accuracy, and always comparable to the best in completeness.

Method	MP3D [2]			3DFront [5]			ScanNet [4]		
	Acc	Cmp	F1	Acc	Cmp	F1	Acc	Cmp	F1
LDI	66.2	<u>72.4</u>	67.4	68.6	46.5	52.7	19.3	28.6	21.5
LDI +C	64.8	55.1	57.7	70.8	45.1	52.4	19.9	32.0	23.3
SAL [1]	66.1	25.5	34.3	80.7	28.5	39.5	51.2	70.0	57.7
UDF	58.7	76.0	64.7	70.1	<u>51.9</u>	57.4	44.4	62.6	50.8
ORF	73.4	69.4	<u>69.6</u>	<u>86.4</u>	48.1	<u>59.6</u>	51.5	58.5	53.7
URDF	74.5	67.1	68.7	85.0	47.7	58.7	<u>61.0</u>	57.8	58.2
DRDF (ours)	75.4	72.0	71.9	87.3	52.6	63.4	62.0	<u>62.7</u>	60.9

scenes: with scene-level evaluation on a high resolution image, a prediction can miss a hidden surface (e.g., the 2nd surface) on every other pixel since the missing predictions will be covered for by hidden surfaces in adjacent rays. Ray-based evaluation, however, requires each pixel to have all hidden surfaces present to receive full credit. Results are reported in Tab. 2.

Table 2: (From Main Paper) Ray Acc/Comp/F1Score on Occluded Points. Thresholds: 0.5m (MP3D [2], 3DFront [5]), 0.2m (ScanNet [4]). DRDF is best on F1 and Acc, and is occasionally 2nd best on Cmp. Gains on occluded points are even larger than the full scene.

Method	MP3D [2]			3DFront [5]			ScanNet [4]		
	Acc	Cmp	F1	Acc	Cmp	F1	Acc	Cmp	F1
LDI	13.9	42.8	19.3	17.8	<u>35.8</u>	22.2	0.5	9.0	2.4
LDI +C	18.7	21.7	19.3	17.7	22.6	19.9	1.1	2.4	3.5
SAL [1]	5.5	0.5	3.5	24.1	4.3	11.4	2.4	38.7	5.6
UDF	15.5	23.0	16.6	29.3	21.3	23.4	1.8	7.8	5.5
ORF	26.2	20.5	21.6	53.2	22.0	<u>31.0</u>	6.6	12.3	11.4
URDF	24.9	20.6	20.7	<u>47.7</u>	23.3	30.2	<u>8.4</u>	11.6	<u>13.8</u>
DRDF (ours)	28.4	<u>30.0</u>	27.3	54.6	56.0	52.6	9.0	<u>20.4</u>	16.0

Rays (Acc/Cmp/F1), All Points. We evaluate each ray independently, measuring Acc/Cmp/F1 on each ray and reporting the mean. Unlike the occluded version of this metric we do not drop the first surface and evaluate using all the ground truth and predicted intersections. This metric has similar properties as the *Occluded* metric but applies the stringent test to all intersections. Results are reported in Tab. 3. We note that, except for SAL on ScanNet [4] which gives higher Cmp. as compared to DRDF at the cost of accuracy where DRDF is the next best; DRDF always outperforms all the baselines on Acc/Cmp/F1

Table 3: (Supplemental Table) Ray Acc/Comp/F1Score on All Points. Thresholds: 0.5m (MP3D [2], 3DFront [5]), 0.2m (ScanNet [4]). DRDF is best on F1 and Acc, and is occasionally 2nd best on Cmp. Gains on occluded points are even larger than the full scene.

Method	MP3D [2]			3DFront [5]			ScanNet [4]		
	Acc	Cmp	F1	Acc	Cmp	F1	Acc	Cmp	F1
LDI	28.8	<u>50.7</u>	35.7	34.1	49.8	39.0	7.3	18.2	11.7
LDI +C	26.8	30.1	27.8	30.6	33.9	31.6	4.7	7.4	8.0
SAL [1]	27.2	19.1	22.4	43.9	25.8	31.6	31.0	60.4	<u>40.8</u>
UDF	32.7	45.3	36.8	51.5	57.1	52.0	27.8	38.9	32.5
ORF	46.4	49.8	<u>46.9</u>	<u>71.8</u>	<u>66.2</u>	<u>67.1</u>	34.1	39.7	36.6
URDF	45.2	46.6	44.8	66.0	56.9	59.3	<u>37.3</u>	39.4	38.7
DRDF	48.3	55.0	50.3	74.9	76.3	74.1	40.3	<u>45.7</u>	43.0

2.2. Effect of different Decodings

We discuss the impact of alternate decoding strategies for baselines in detail here. For the sake of brevity we reported numbers only on Scene-F1 score in the text of the main paper. Here we report the numbers on all the metrics for baseline and their alternate decoding strategies in Tab 4. We first describe UDF, followed by URDF and then followed by ORF.

UDF. We tried two other decoding strategies with UDF namely, absolute thresholding (*UDF + Th.*) and Sphere tracing followed by gradient based optimization (*UDF + Sph.*) as proposed by Chibane *et al.* [3]. We observe as reported in the main paper that these two strategies do slightly worse on Scene F1 Score than our best reported strategy of using `scipy.argrelextrema` to find minimas of the distance function along the ray.

On other metrics of Ray based Acc/Cmp/F1 we observe that our strategy does especially well on discovering occluded regions. We speculate that using absolute thresholding is especially bad because of the behavior of global unsigned distance under uncertainty. Moreover, due to the model’s inability to mimic the GT URDF we find that using sphere tracing as proposed by Chibane *et al.* [3] is not as effective.

URDF. We use three alternate decoding strategies to best recover the surface locations for model trained with unsigned ray distance. First, we use absolute thresholding (*URDF + Th.*) on the predicted distance by considering all points with value distance prediction $\leq \tau$. We choose τ by cross-validation. Second, we use the numerical gradient to find the zero crossings of the gradient functions hence detecting the minimas (*URDF + Grd.*). Thirdly, we use sphere tracing followed by gradient based optimization from Chibane *et al.* [3] (*URDF + Sph.*). As reported in the

Table 4: (Supplemental Table) Effect of different decodings.
 Thresholds: 0.5m (MP3D [2]). **Bold** is best per column and section (created by horizontal lines). We compare alternate decoding strategies for baseline methods and report their performance on the three metrics ; Scene Acc/Cmp/F1, Ray Acc/Cmp/F1 All, Ra Acc/Cmp/F1 Occluded

Method	Scene			Ray All			Ray Occluded		
	Acc	Cmp	F1	Acc	Cmp	F1	Acc	Cmp	F1
UDF + Th.	79.3	49.7	58.8	46.2	27.6	32.9	18.0	2.6	5.2
UDF + Sph.	50.8	32.8	37.5	19.3	22.6	20.1	11.4	2.1	4.7
UDF	58.7	76.0	64.7	32.7	45.3	36.8	15.5	23.0	16.6
URDF + Th.	82.5	55.1	63.3	56.7	47.7	50.1	16.6	30.6	18.6
URDF + Grd.	48.5	75.8	57.4	24.6	50.9	32.2	11.4	37.2	16.1
URDF + Sph.	59.1	69.4	62.4	45.9	46.5	44.8	23.8	15.3	16.7
URDF	74.5	67.1	68.7	45.2	46.6	44.8	24.9	20.6	20.7
ORF + Sngle.	70.9	62.9	64.7	36.6	37.5	36.2	22.0	18.9	18.9
ORF	73.4	69.4	69.6	46.4	49.8	46.9	26.2	20.5	21.6
DRDF (ours)	75.4	72.0	71.9	48.3	55.0	50.3	28.4	30.0	27.3

main text all these strategies perform worse on Scene F1 score with regards to our strategy that does non-maximum suppression on the thresholded data by finding connected components of the ray that have predicted distance below a tuned-constant τ .

On other metrics of Ray based Acc/Cmp/F1 we observe that URDF with our decoding strategy outperforms all alternate choices on considerably on the occluded points. URDF + Th. and URDF + Grad. tend to high F1 scores on occluded points but this is due high completion scores that these methods have as compared to their accuracy. URDF + Sph. does reasonably well on the occluded points but is outperformed likely as it assumes that the predicted URDF behaves like a GT URDF.

ORF. Our choice of decoding strategy for ORF is based on the fact that ORF predicts an onset and a offset zero crossing. We keep the average of onset and the offset crossings when we find pairs and keep the single crossing otherwise. An alternate decoding strategy is to only keep only one of the zero crossings. We report the scene F1 score for keeping on a single zero crossing under *ORF + Sngl.* and see that it under performs our strategy by (4.9 points). Additionally our ORF decoding strategy also outperforms on Ray based metrics.

3. Dataset Details

Matterport3D [2]. Apart from the details mentioned in the main paper. For matterport we clip scene to 8 meters in depth from the camera so only considering the mesh that is within 8m to compute the locations of ground truth intersections. Such a large range is necessary as matterport is

a collection of scenes and this allows other models to run additional rooms behind walls.

3DFront [5]. Apart from the details mentioned in the main paper. For 3DFront also we clip scene to 8 meters in depth from the camera so only considering the mesh that is within 8m to compute the locations of ground truth intersections. Such a large range is necessary as matterport is a collection of scenes and this allows other models to run additional rooms behind walls.

ScanNet [4]. We use splits from [4] (1045/156/312 train/val/test) and randomly select 5 images per scene for train set, and 10 images per scene for val/test set. We then sample to a set of 33K/1K/1K images per train/val/test. For ScanNet we clip the scene t 4 meters in depth from the camera so only considering mesh that is within 4m to compute the locations of ground truth intersections. We use a smaller range than Matterport3D [2] and 3DFront [5] because this dataset mostly has individual rooms for which this range suffices.

4. Video Results & Interactive Demo

4.1. Video Results

We provide three video files with results from our models. These videos show the outputs of our model and compare them to the ground truth and baselines by showing salient features at different instances in video frames.

- `main_paper.mp4`. Shows the qualitative results from Fig 6, and Fig 7 of the main paper in order of their appearance. We highlight salient regions our model similar to the zoom-ins in the main paper to qualitatively compare the outputs. The first part of the video compares the DRDF outputs with ground truth and the second part of the video compares against various baselines. This video contains *all* the qualitative examples in the main paper.
- `additional.mp4`. This video shows additional qualitative examples in addition to the main qualitative examples shown. It is also divided into two parts where the first part compares against ground truth while the second part compares against outputs of other baseline methods.
- `supp_qual.mp4`. This video shows six samples from the qualitative figures shown in the supplemental in Fig. 7, 9, 11 (2 samples from each dataset) and compares the outputs against the ground truth.

4.2. Interactive Demo

We provide three outputs of DRDF from the main paper and embed them inside the HTML as an interactive demo to qualitatively assess our outputs and compare against the GT. The demo allows us to view the outputs from the given input image (left most column on the demo) and compare with GT(middle column on the demo) with the prediction (right most column on the demo) Inside the folder

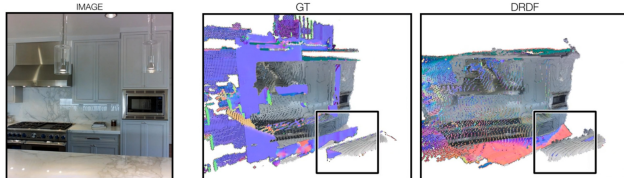


Figure 1: Qualitative Video. Screen Capture from `main_paper.mp4`. Our video shows model outputs and a highlight box (red/black) describing regions of interest and salient differences between methods. Our supplementary contains three videos of results each showcasing a different set of examples. a) `main_paper.mp4` has all the results from the main paper and we highly encourage watching this. b) `additional.mp4` has more result showcasing performance with respect to other baselines, and ground-truth c) `supp_qual.mp4` has video results for samples in the supplementary PDF



Figure 2: Interactive Demo. Screen Capture of interactive demo. We present an interactive demo of selected outputs from the main paper, allowing explorations from more camera viewpoints not explored completely in the video trajectory. Please open the `model_vis.html` in your web-browser (works best with Google Chrome and Firefox).

`interactive_demo` is a file `model_vis.html`. Open this file in a web browser (best viewed in Google Chrome or Firefox) to see the interactive demo of the output from our model.

5. Distance Functions Under Uncertainty

This section, §5, presents all the results that are important to understand the differences in behavior of the ray-based distance function and we directly state them. All the derivations for these results are in §7 (towards the end of this document).

We analyze a single intersection along ray and behavior of distance functions with it. We will start with the setup,

then show key results for different ray distance functions.

Setup. We assume we are predicting a distance-like function along a ray. Given surface geometry the ray intersects, the distance function’s value is a function of the distance z along the ray.

We analyze the case of uncertainty about a single intersection. We assume the intersection’s location is a random variable S that is normally distributed with mean μ (the intersection’s location) and standard deviation σ . Throughout, WLOG, we assume the intersection is at $\mu = 0$ for convenience. This considerably simplifies some expressions, and can be done freely since we are free to pick the coordinate system. The rest follows the main paper. Let $p(s)$ denote the density and $\Phi(s)$ denote the CDF for samples from S . We assume that the distance to the second intersection is $n \in \mathbb{R}^+$, which we will assume is not a random variable for simplicity (i.e., the second intersection is at $S + n$, which is normally distributed with mean n and standard deviation σ).

Given a value s for the intersection location, we can instantiate the distance function. We denote the value of the distance function at z if the intersection is at s as $d(z; s) : \mathbb{R} \rightarrow \mathbb{R}$ that maps a location z on the ray to a (possibly signed) distance. The distance if s is at the real location is $d(z; 0)$.

Training. During training, a function approximator is trained to minimize a loss function that measures the distance between its predictions and the ground-truth. The optimal behavior of this function approximator is to output the value that minimizes the loss function. One critical value is the *expected* value of the distance function

$$E_S[d(z; s)] = \int_{\mathbb{R}} d(z; s)p(s)ds. \quad (1)$$

Eqn. 1 is important for various loss functions:

- Mean Squared Error (MSE): $E_S[d(z; s)]$ is the optimal value when minimizing the MSE.
- Cross-Entropy: If $d(z; s)$ is an indicator function (i.e., producing either 1/positive or 0/negative), then $E_S[d(z; s)]$ minimizes the cross-entropy loss as well. This follows from the fact that $E_S[d(z; s)]$ is the chance z is positive, and a cross-entropy loss is minimized by matching frequencies.
- L1 Loss: The median (rather than the mean) is the optimizer for the L1 loss. However, the median and mean are the same for symmetric distributions. If one calculates $d(z; S)$ (where S is the random variable rather than a particular value), one obtains a new random variable. If this distribution is symmetric, then the mean and median are the same, and therefore $E_S[d(z; s)]$ minimizes the L1 loss too. In practice (see

§5.5, Fig. 6), we empirically find that any deviations between the mean and median are small, and thus the mean and median are virtually identical almost all of the time.

We can think of this setting from two angles:

1. $E_S[d(z; s)]$ as a 1D function of z . In our setting, our neural networks are incentivized to minimize their distance from this value; the S is implicit. This is the primary way that we look at the problem since it gives us a function of z . We can then do things like compute $\frac{\partial}{\partial z}$.
2. $d(z; S)$ as a distribution over the distance for some fixed z . We use this angle to explain why the mean and median are similar in most cases.

We can then analyze the *expected* distance function ($E_S[d(z; s)]$) for various distance functions, as well as the derivative $\frac{\partial}{\partial z} E_S[d(z; s)]$, and the difference between the expected distance function and the underlying distance function ($E_S[d(z; s)] - d(z; s)$). We plot distance functions and their difference from the ground truth in Figs. 3, 4.

The expected distance functions usually have two regimes: a regime in which they closely mimic the underlying distance function and a regime in which there are substantial distortions that are usually dependent on the level of uncertainty. These distance functions vary in where the distortions occur – some have them near the intersection and others have them far away. When analyzing the expected functions, these regimes are caused by the PDF p going to 0 or the CDF Φ going to either 0 or 1.

5.1. Signed Ray Distance Function (SRDF)

Ignoring the second intersection, which has limited impact near the first intersection, the signed ray distance function (SRDF) is

$$d_{\text{SR}}(z; s) = s - z \quad (2)$$

assuming WLOG that $z < s$ is outside and positive. The expected distance function and its derivative are

$$E_S[d_{\text{SR}}(z; s)] = -z, \quad \frac{\partial}{\partial z} E_S[d_{\text{SR}}(z; s)] = -1. \quad (3)$$

Considering the second intersection at n creates additional terms in the expected SRDF that are negligible near 0, specifically

$$(2z - n)\Phi\left(z - \frac{n}{2}\right) + 2 \int_{z-\frac{n}{2}}^{\infty} sp(s)ds. \quad (4)$$

Finding intersections. Finding the intersection is straightforward, since it is a zero-crossing and the expected function behaves like the actual function near the intersection.

5.2. Unsigned Ray Distance Function (URDF)

Likewise ignoring the second intersection, the unsigned ray distance function (URDF) is

$$d_{\text{UR}}(z; s) = |s - z|. \quad (5)$$

The expected distance function consists of three terms that trade off in magnitude over the values of z :

$$E_S[d_{\text{UR}}(z; s)] = z\Phi(z) + -z(1 - \Phi(z)) + 2 \int_z^{\infty} sp(s)ds, \quad (6)$$

which induces three regimes: z when $z \gg 0$, $-z$ when $z \ll 0$, and a transitional regime near 0. The trade off between the regimes is controlled by Φ and $\int_z^{\infty} sp(s)ds$ (which is ≈ 0 when $z \gg 0$ or $z \ll 0$). The function's minimum is 0, but the minimum value of expectation is $\sigma\sqrt{2/\pi}$. The derivatives is

$$\frac{\partial}{\partial z} E_S[d_{\text{UR}}(z; s)] = 2\Phi(z) - 1, \quad (7)$$

which again has three regimes: -1 for $z \ll 0$, $+1$ for $z \gg 0$, and a transitional regime near 0. Thus, the expected URDF has distance-function-like properties away from the intersection.

The second intersection. Like the SRDF, accounting for the second intersection leads to a more complex expression. The expected second intersection also includes the terms

$$(n - 2z)\Phi\left(z - \frac{n}{2}\right) + \int_{-\infty}^{z-\frac{n}{2}} sp(s)ds, \quad (8)$$

which are negligible near 0 and produce distortion at the half-way point $n/2$.

Finding intersections. Finding the intersection is challenging again due to how σ substantially alters the function at the minimum. Thresholding is challenging because the minimum value is uncertainty-dependent; searching for where the gradient approaches zero is difficult because the expected value is substantially more blunted.

5.3. (Proximity) Occupancy Ray Function (ORF)

A traditional occupancy function (i.e., inside positive, outside negative) is impossible to train on non-watertight meshes. One can instead train an occupancy network to represent the presence of surface. The occupancy ray function (ORF) is:

$$d_{\text{ORF}}(z; s) = \mathbf{1}_{\{x:|x-s|<r\}}(z). \quad (9)$$

Its expectation is the fraction of the density within a radius r of z , or

$$E_S[d_{\text{ORF}}(z; s)] = \Phi(z + r) - \Phi(z - r), \quad (10)$$

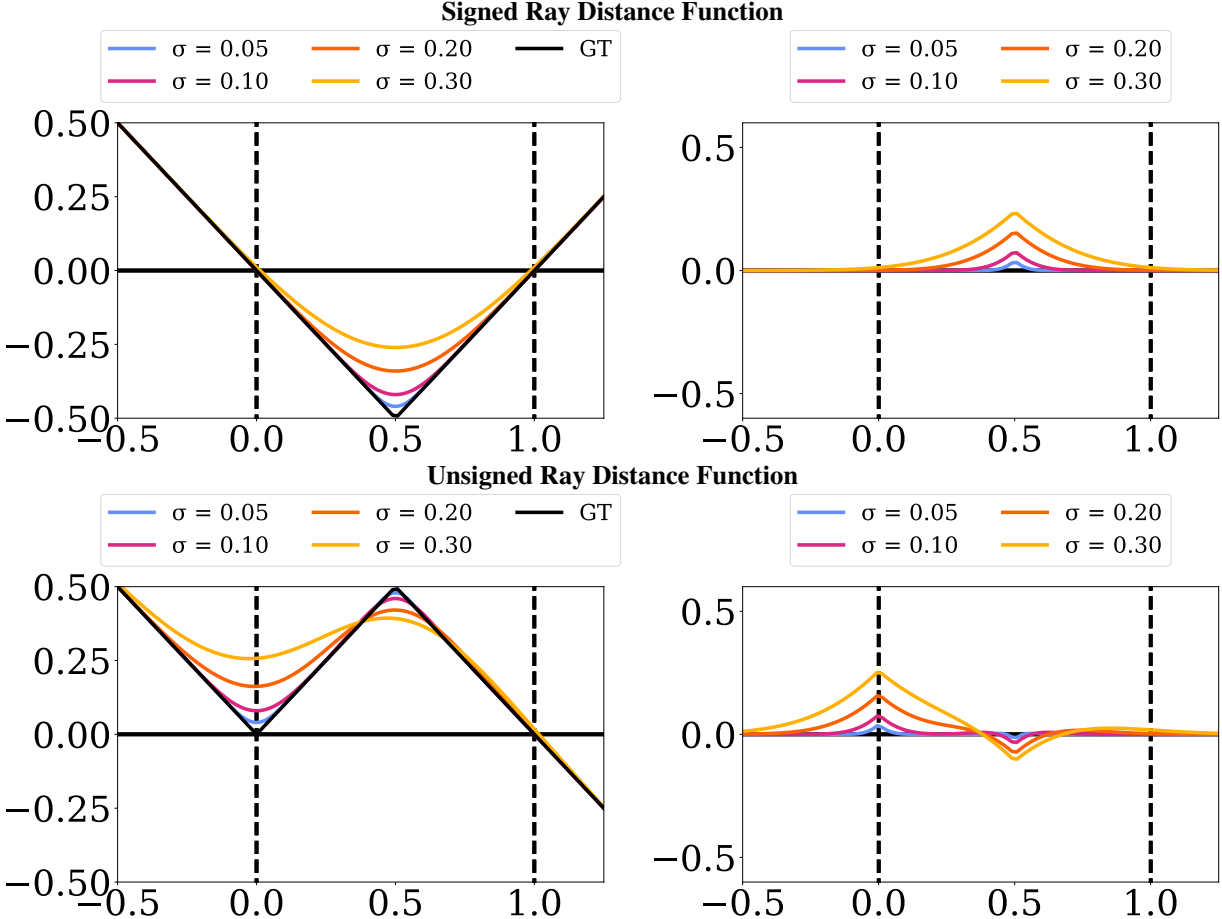


Figure 3: Expected distance functions and their deviation from the real distance function. We plot the expected distance function $E_S[d(z; s)]$ (**left**) and the residual between the expectation and the real distance function $E_S[d(z; s)] - d(z; s)$ (**right**). In each case, we plot the expectation for four σ . In all cases the next intersection is $n = 1$ away, and so if the units were m , one could think of the noise as 5, 10, 20, and 30cm. For the signed and unsigned distance functions, we plot the full versions that also account for the next intersection.

which has a peak at $z = 0$.

Finding intersections. Finding the intersection is challenging due to the strong interaction between the radius r and the uncertainty σ . For instance, suppose one looks for when the occupancy probability crosses a threshold τ (e.g., $\tau = 0.5$). This crossing may never happen, since if $r = \frac{1}{2}\sigma$, then $\max_z E_S[d_{\text{ORF}}(z; s)] \approx 0.38$. Moreover, setting a global threshold is difficult: the distance from which the τ -crossing is from the true peak depends entirely on σ . On the other hand, looking for a peak is also challenging: if $r > 3\sigma$, then many values are near-one and roughly equal, since $(z + r, z - r)$ will cover the bulk of the density for many z ; if $r < \sigma$, then the peak's magnitude is less than one.

5.4. Directed Ray Distance Function

The directed ray distance function is

$$d_{\text{DRDF}}(z; s) = \begin{cases} s - z & : z \leq n/2 + s \\ n + s - z & : z > n/2 + s. \end{cases} \quad (11)$$

Despite the complexity of the function, the expectation is relatively a straightforward

$$E_S[d_{\text{DRDF}}(z; s)] = n\Phi\left(z - \frac{n}{2}\right) - z, \quad (12)$$

which can be seen to have three regimes: $-z$ when $z \ll n/2$, $n - z$ when $z \gg n/2$, and a transition near $n/2$. These regimes are traded off by whether $\Phi(z - \frac{n}{2})$ is 0, 1, or something in between. Moreover, so long as $p(z - n/2) \approx 0$ (i.e. the uncertainty is smaller than the distance to the next intersection), the function has a zero-crossing at ≈ 0 – note that

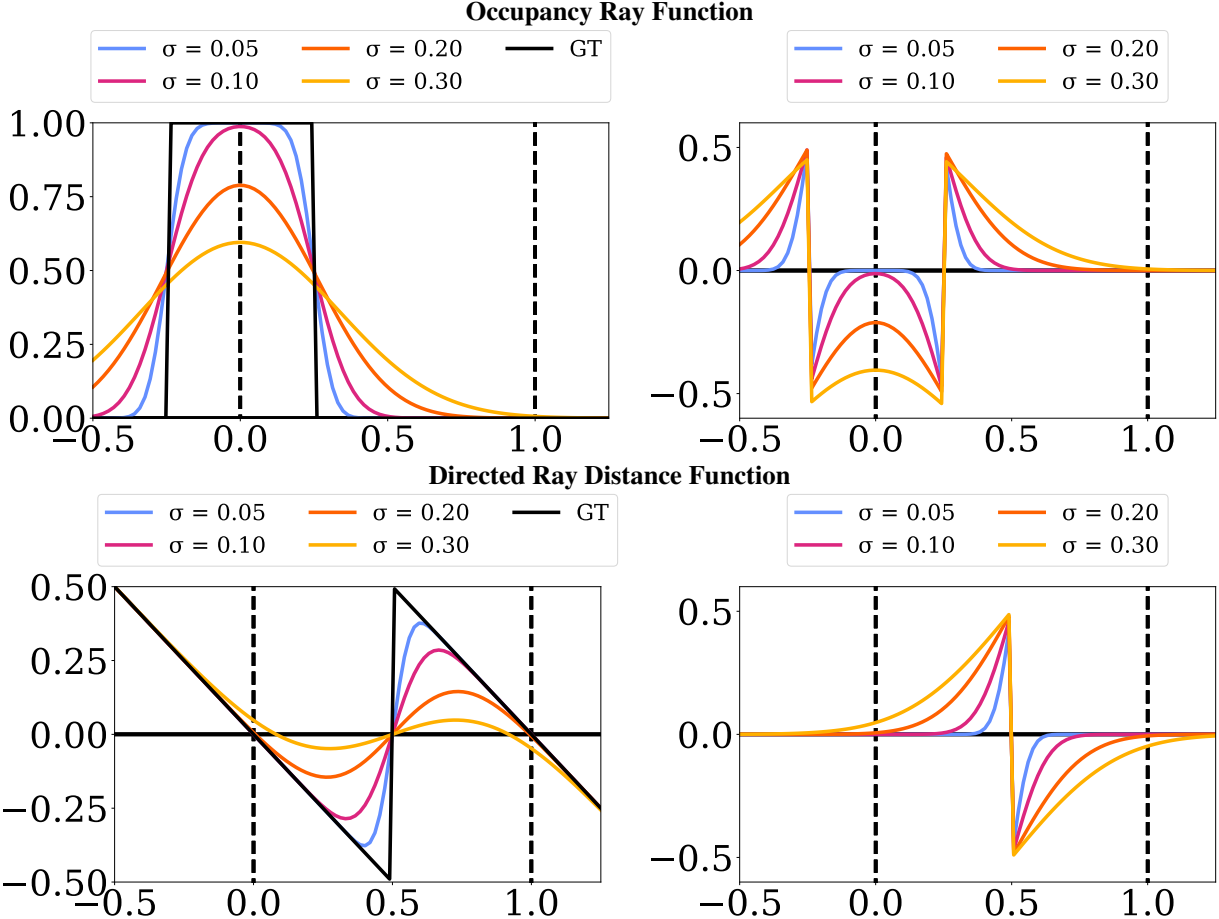


Figure 4: Expected distance functions and their deviation from the real distance function. We plot the expected distance function $E_S[d(z; s)]$ (**left**) and the residual between the the expectation and the real distance function $E_S[d(z; s)] - d(z; s)$ (**right**). In each case, we plot the expectation for four σ . In all cases the next intersection is $n = 1$ away, and so if the units were m , one could think of the noise as 5, 10, 20, and 30cm.

if one sets $n = 1$ (fixing the scale) the value at $z = 0$ is $\Phi(-1/2)$. The derivative of the expected distance function is

$$\frac{\partial}{\partial z} E_S[d_{DRDF}(z; s)] = np \left(z - \frac{n}{2} \right) - 1, \quad (13)$$

which again has two regimes: -1 when $p(z - \frac{n}{2}) \approx 0$, which happens when z is far from $\frac{n}{2}$, which in turn happens for $z \ll n/2$ and $z \gg n/2$; and a transitional regime near $n/2$, where the derivative is not -1 .

The location of the zero-crossing is controlled by σ . For most σ of interest, the zero-crossing is nearly at zero. This value can be computed as the \hat{z} such that $n\Phi(\hat{z} - \frac{n}{2}) - \hat{z} = 0$. We plot the location of the zero-crossing \hat{z} as a function of σ in Fig. 5, assuming $n = 1$ (note that n scales with σ). \hat{z} first crosses 0.01 (i.e., 1cm error) when $\sigma = 0.21$, or when the standard deviation of the uncertainty about surface location is 20% of the distance to the next intersection. The DRDF does break down at for large σ (e.g., $\sigma = 0.3$, where it is off

by ≈ 0.1 .

Finding intersections. Finding the intersection is made substantially easy because the uncertainty-dependent contortions of the function are pushed elsewhere. The discontinuity at $n/2$ does create a phantom zero-crossing, but this is easily recognized as a transition from negative to positive.

5.5. Median vs Expectation

The above analysis is in terms of the expected distance function since this is easiest to derive. However, the median distance function closely tracks the expected distance function for the distance functions we study.

Empirical results. Empirically, the results for the median are virtually identical. We sample intersections independently from the distributions shown in Fig. 6, where the variance is depth-dependent. We then numerically calculate the expectation/mean and the median over 1M samples

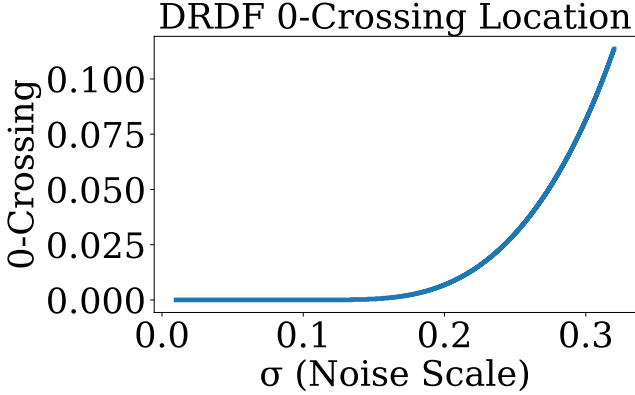


Figure 5: Location of the zero crossing of the DRDF as a function of σ (for $n = 1$; this scales with n). The zero-crossing is virtually at zero until σ becomes a substantial fraction of the distance to the next intersection. The smallest σ for which the zero-crossing location exceeds 0.01 (i.e., 1cm if $n = 1\text{m}$) is 0.21; for 0.05, it is 0.27.

from this distribution. The plots are virtually identical. Two small differences are visible: the median URDF is slightly smaller than the mean URDF near intersections, and the median DRDF more closely resembles the ground-truth DRDF by better capturing the discontinuity. We do not plot the ORF since cross-entropy training minimizes the mean.

Analysis. These empirical results occur because if we treat the distance function at a location z as a random variable, then the mean and median are similar. More specifically, for a fixed z , if we plug in the random variable S into the distance function $d(z; S)$, we can analyze a new random variable for the distance to the surface at location z . For instance, the SRDF at location z is $S - z$ if we ignore the second intersection; in turn, $S - z$ is normally distributed with mean $-z$. The mean and median are identical for the normal since it is symmetric.

URDF. A more involved case is the URDF. The URDF at location z is $|S - z|$, which is a folded normal with mean $-z$ and standard deviation σ (with the σ inherited from the uncertainty about the intersection location). We'll focus on bounding the gap between the mean and median value at each location.

To the best of our knowledge, there is no closed form expression for the median, and Chebyshev gives vacuous bounds, and so we therefore compute it numerically (using the fact the the median of the folded normal is the m such that $\Phi_z(m) = 0.5 + \Phi_z(-m)$ where Φ_z is the CDF of a normal centered at z). Note that when z is far from the intersection, the folded normal and normal are virtually identical – close to none of the normal's density is on negative values. In general, one can bound the gap between mean and median by numerical search over different possible values for

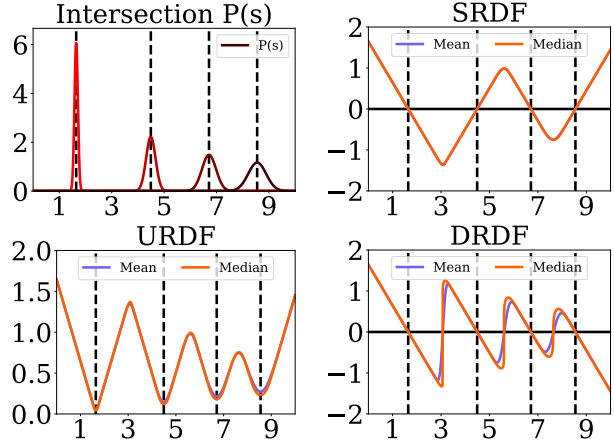


Figure 6: Median-vs-Expectation/Mean for UDF, SDF, and DRDF. We sample intersections from a set of per-intersection distributions (top left). We then compute at each point along the ray, the mean and median distance function. The mean and median are virtually identical apart from a slight shift in the UDF minima, and sharpening in the DRDF near the discontinuity.

z. For $\sigma = 1$, the largest difference is ≈ 0.135 . Changing σ scales this: $\sigma = 0.5$ yields ≈ 0.067 . Note that the minimum is $\sigma\sqrt{2/\pi} = 0.797\sigma$, so for $\sigma = 1$, the median's minima is ≥ 0.663 . Thus, in general, the median has to be quite close to the mean.

DRDF. The DRDF has a larger distortion near $\frac{n}{2}$ because the random variable near $\frac{n}{2}$ is bimodal. The mean splits the difference between the modes while the median sharply transitions depending on which mode is more likely. This discrepancy, however, occurs far from the intersection and is therefore not of concern. For z near the intersection, the resulting random variable resembles a normal distribution.

5.6. Unsigned Distance Function to A Plane in 3D

Suppose we are given a plane consisting of a normal $\mathbf{n} \in \mathbb{R}^3$ with $\|\mathbf{n}\|_2 = 1$ and offset o (where points \mathbf{x} on the plane satisfy $\mathbf{n}^T \mathbf{x} + o = 0$). Then $d_U(\mathbf{x}; \mathbf{n}, o)$ is the unsigned distance function (UDF) to the plane, or

$$d_U(\mathbf{x}) = |\mathbf{n}^T \mathbf{x} + o|. \quad (14)$$

Suppose there is uncertainty about the plane's location in 3D. Specifically, let us assume that the uncertainty is some added vector $\mathbf{s} \sim N(\mathbf{0}, \sigma^2 \mathbf{I})$ where \mathbf{I} is the identity matrix and $\mathbf{0}$ a vector of zeros. Then the expected UDF at \mathbf{x} is

$$E_{\mathbf{s}}[d_U(\mathbf{x}; \mathbf{s})] = \int_{\mathbb{R}^3} |\mathbf{n}^T (\mathbf{x} + \mathbf{s}) + o|(\mathbf{s}) ds. \quad (15)$$

This ends up being the expected URDF, but replacing distance with point-plane distance. Specifically, if $p = |\mathbf{n}^T \mathbf{x} +$

$o|$, then

$$E_{\mathbf{s}}[d_U(\mathbf{x}; \mathbf{s})] = p\Phi(p) - p(1 - \Phi(p)) + 2 \int_p^\infty sp(s)ds. \quad (16)$$

Thus, the minimum value remains $\sigma\sqrt{2/\pi}$.

One nuance is that the rate at which p changes is different for different rays through the scene and is proportional to the cosine between the normal \mathbf{n} and the ray. So the function is stretched along its domain.

6. Qualitative Results

We show qualitative results on *randomly sampled* images from the test set on 3 datasets. In Fig. 7 and Fig. 8 we compare on Matterport3D [2] with respect to ground truth and baselines. Similarly we show results for 3DFront [5] on Fig. 9 and Fig. 10. Results for in ScanNet [4] in novel views in Fig. 11 and comparison against baseline is in Fig. 12. We show some selected results from these random samples (2 per dataset) in the `supp_qual.mp4`. We recommend watching this video.

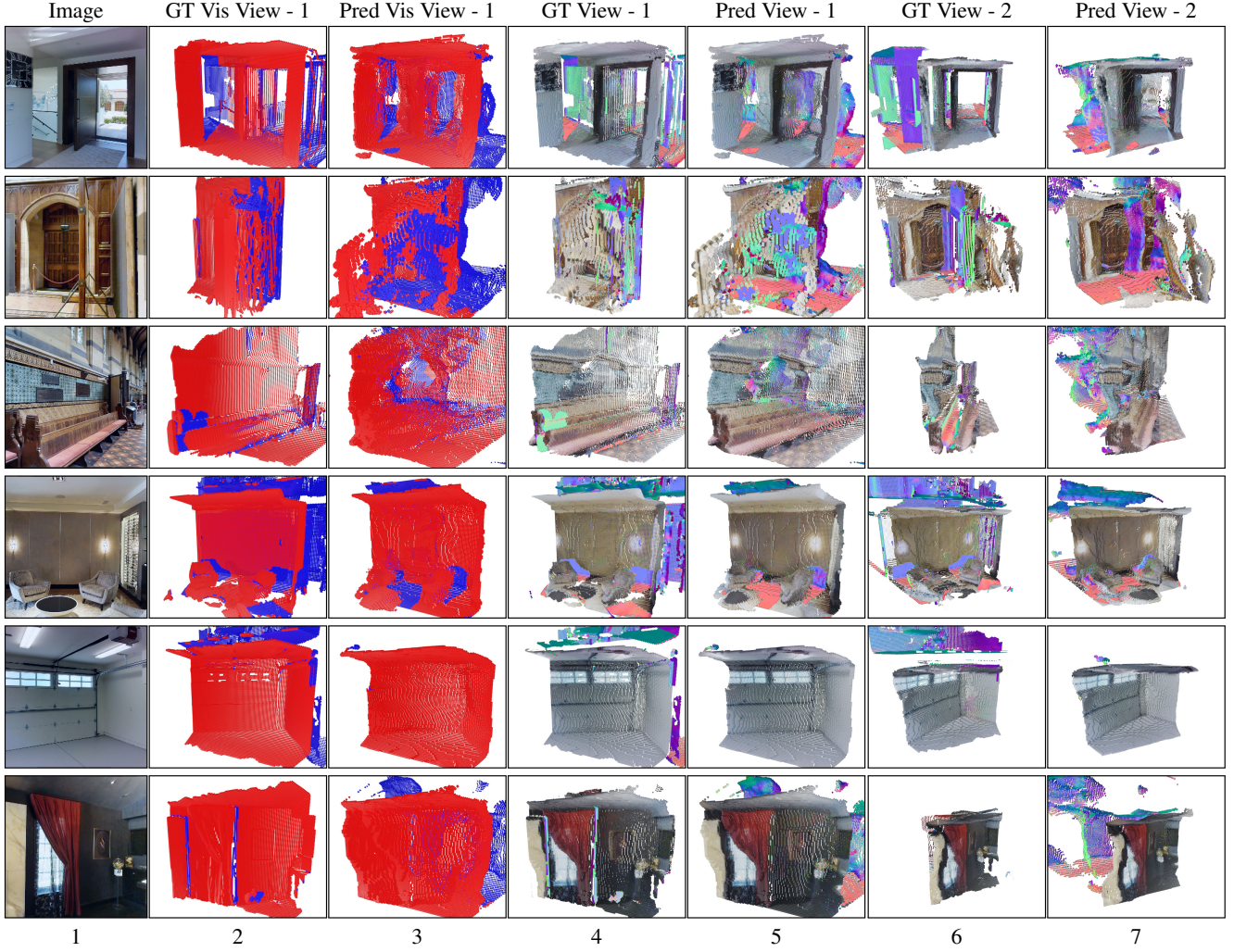


Figure 7: Matterport Novel Views We randomly sample examples from the test set and show results and show generated 3D outputs in a new view for them in novel view. Video results for Row 1 and Row 4 are present in the `supp_qual.mp4`. Cols 2 & 3 show regions in **red as visible** in camera view and **blue as occluded** in camera view. We colors the **visible regions** with image textures and the **occluded regions** with surface normals (Flag scheme from camera inside a cube) in Col 4, 5, 6, 7. We observe that our model is able to recover parts of the occluded scene shown in blue and colored with surface normal map; floor behind the wall (row 1), walls and floor behind couch (row 4).

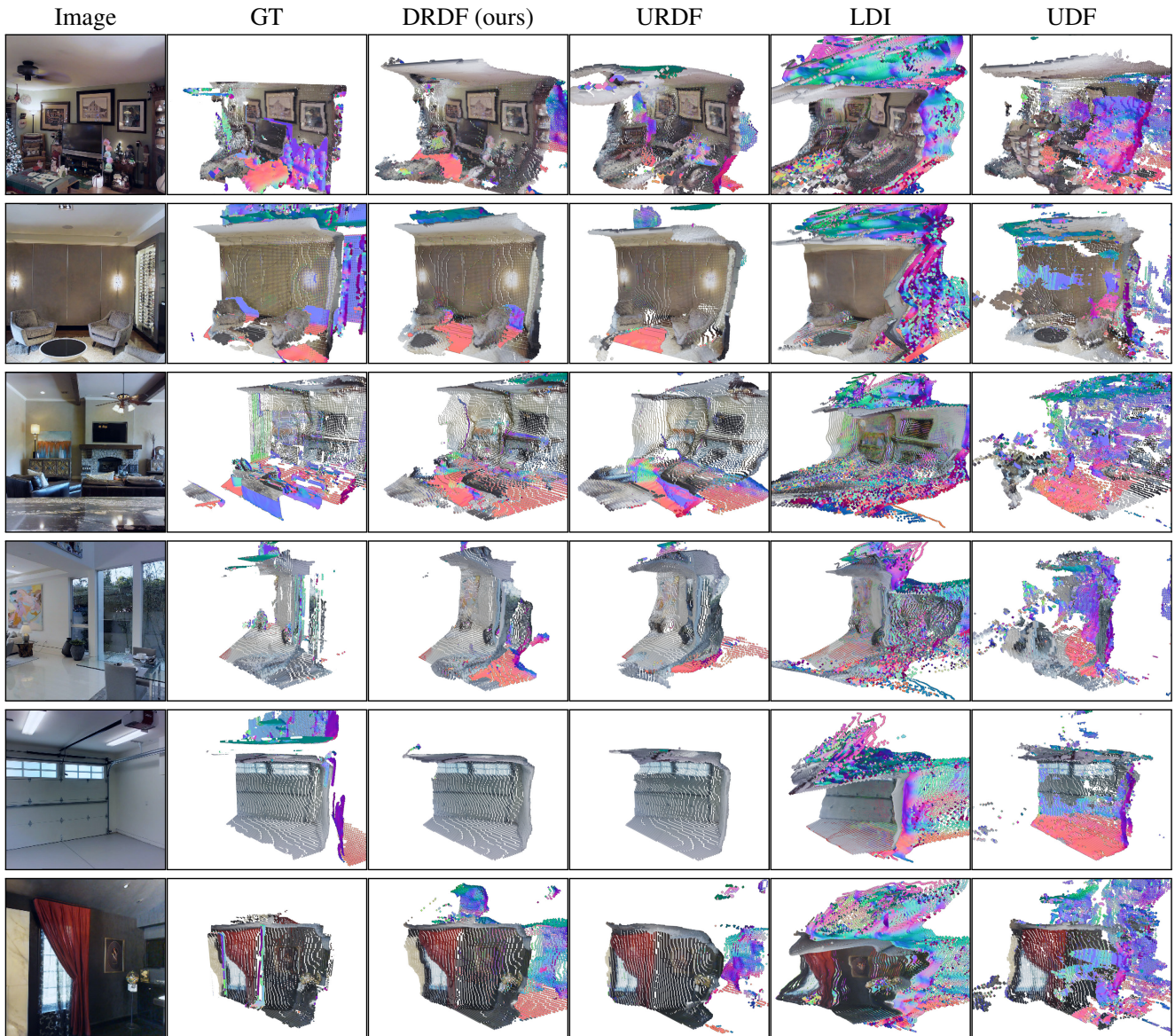


Figure 8: Matterport Comparison with Baselines We randomly sample from the test set and show results comparing DRDF to other baselines. DRDF shows consistently better results as compared to UDF and LDI. Both UDF and LDI have blobs and inconsistent surfaces in output spaces (all rows). URDF always is unable to recover hidden regions (row 3 behind the couch on the right), URDF is missing the floor on lower right (row 4) as compared to DRDF.

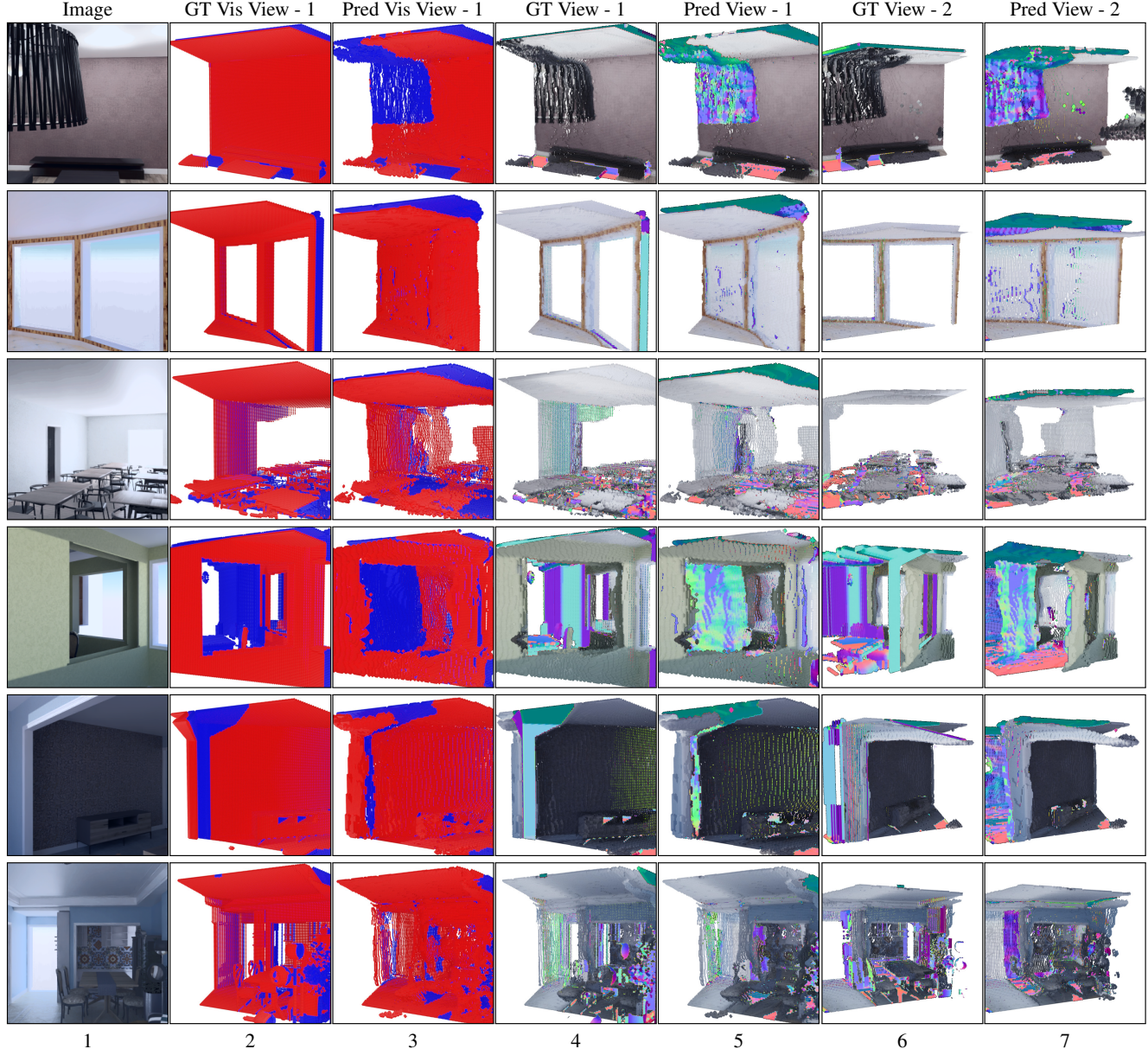


Figure 9: 3DFront Novel Views We randomly sample examples from the 3DFront [5] test set and show results. Video results are available for row 2, 6 in the `supp_qual.mp4`. We observe our model recovers portion of floor occluded by the table (row 2, bottom right of the image) ; our model is also able to identify small occluded regions in a complicated scene (row 6)

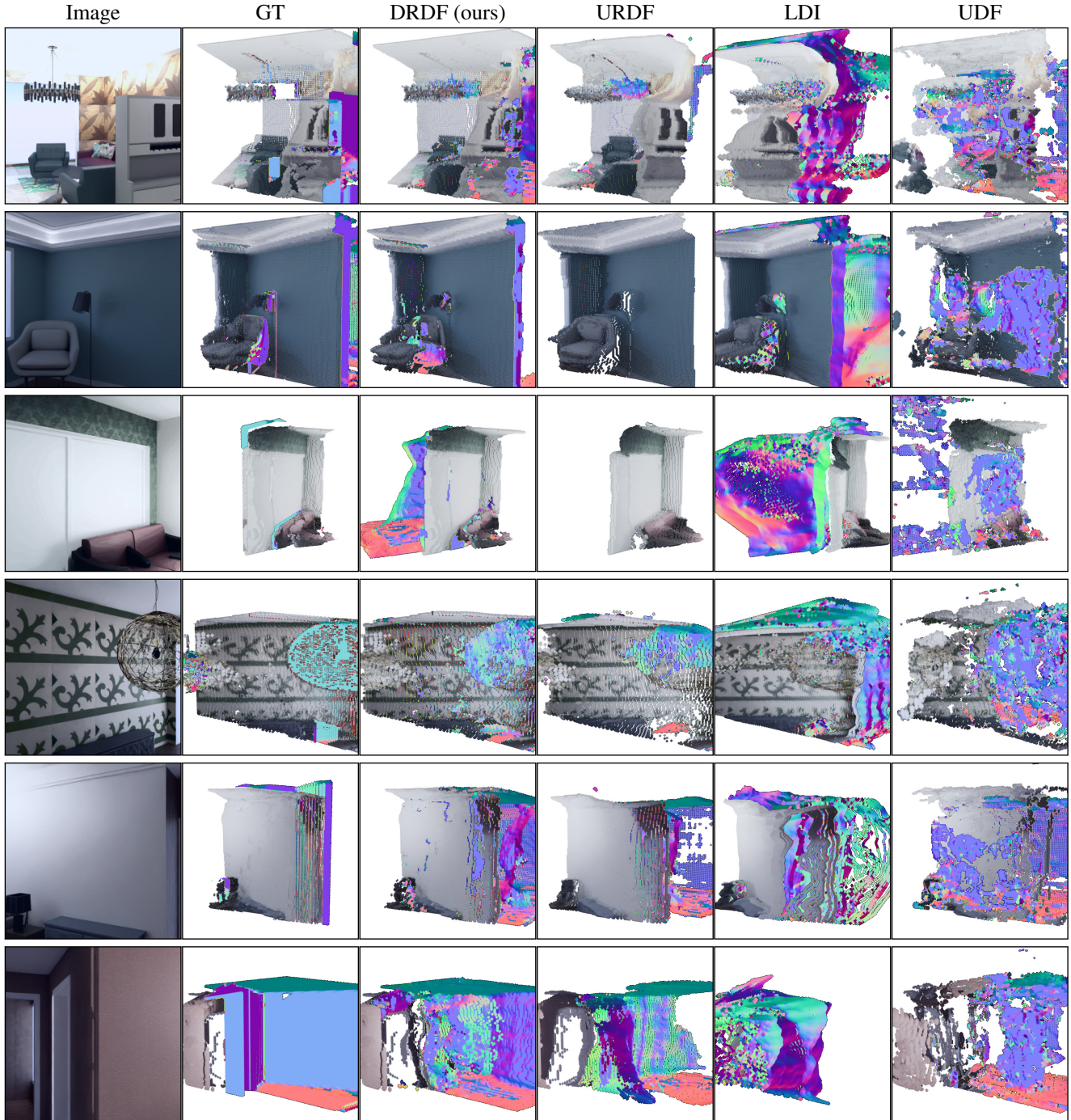


Figure 10: 3DFront Comparison with Baselines We randomly sample samples from the test set and show results comparing DRDF to other baselines. DRDF shows consistently better results as compared to UDF and LDI. Both UDF and LDI have blobs and inconsistent surfaces in output spaces (all rows). URDF always is unable to recover hidden regions (row 2 behind the couch on the right) while DRDF does. DRDF also speculates another room in the scene (row 3, 5)

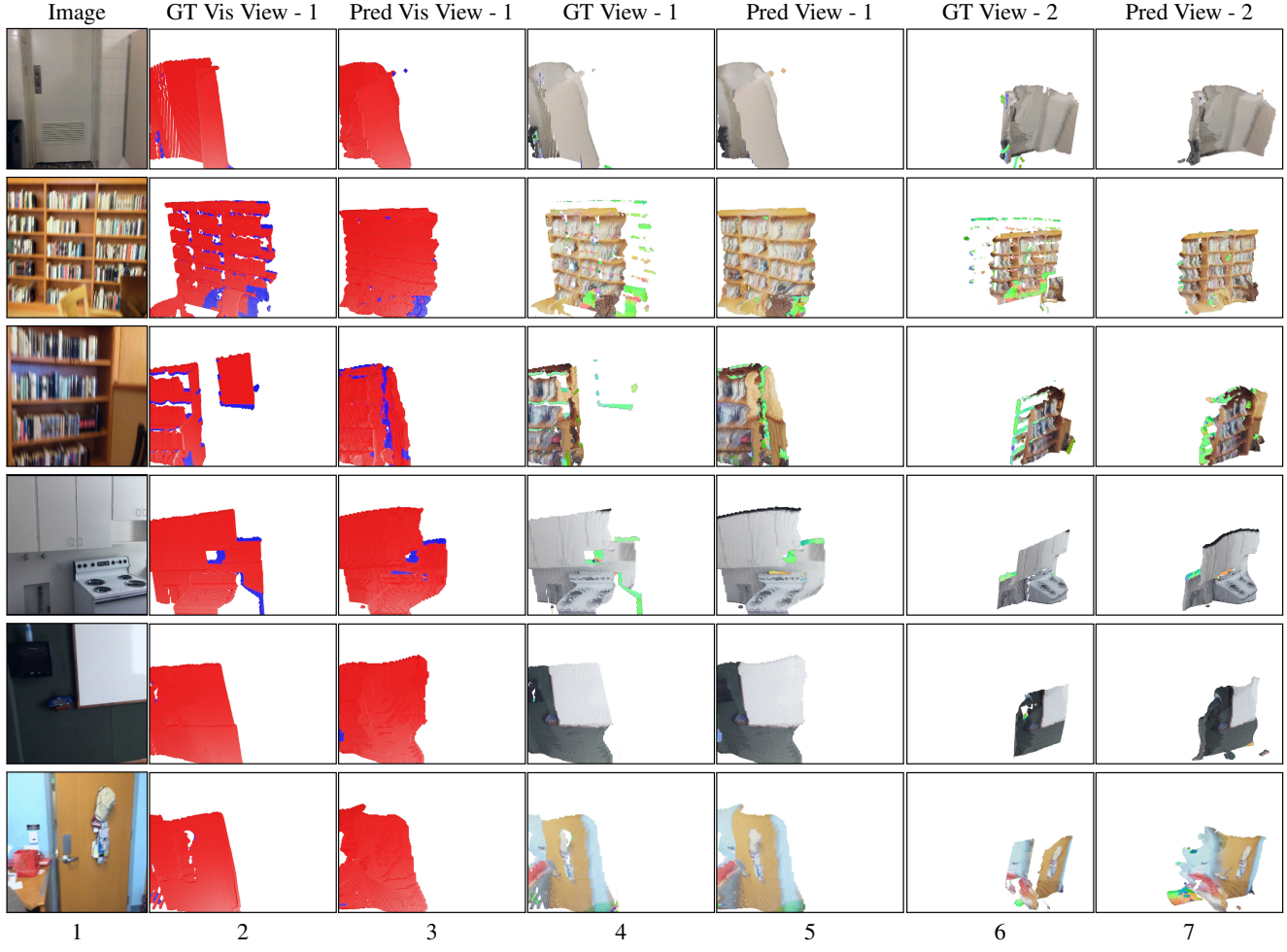


Figure 11: ScanNet Novel Views We randomly sample examples from the ScanNet [4] test set and show results. Video results are available for row 2, 4 in the `supp_qual.mp4`. We observe our model recovers portion of wall occluded by the chair (row 2, bottom right of the image View 1) ; ScanNet does not have lot of occluded surfaces as we can see from ground-truth and hence a lot of regions in novel views are visible in the camera view.

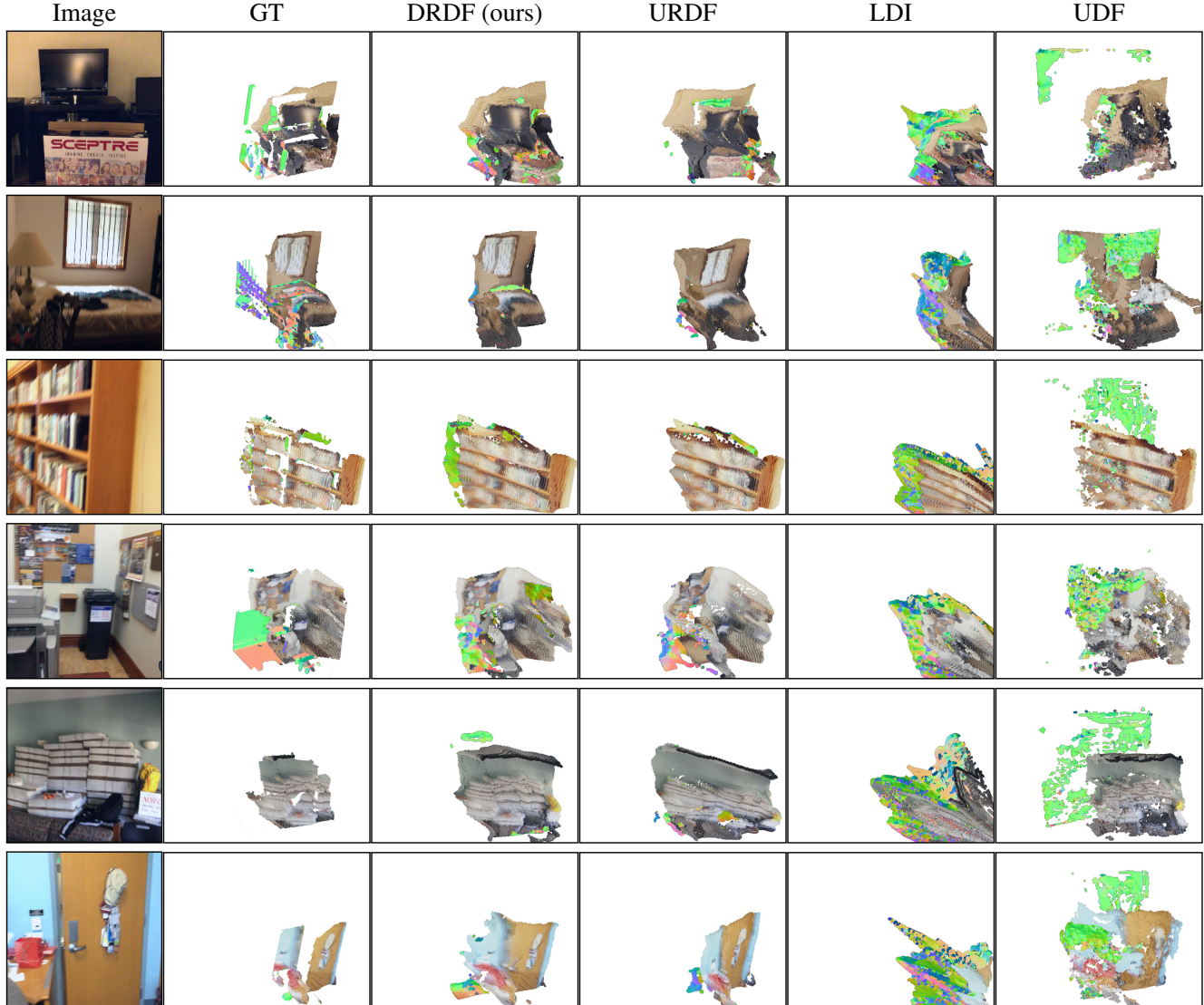


Figure 12: ScanNet Comparison with Baselines We randomly sample samples from the test set and show results comparing DRDF to other baselines. DRDF shows consistently better results as compared to UDF and LDI. Both UDF and LDI have blobs and inconsistent surfaces in output spaces (all rows). DRDF outputs look more closer to the ground-truth as compared to URDF (row 4)

7. Derivations

For completeness, we show the derivation of some of the results presented in §5. This is meant to help in verifying the solutions or deriving the solution for another function. Assume $S \sim N(0, \sigma)$ with density $p(s)$ and CDF $\Phi(s)$.

Useful identities:

1. $\int_{-\infty}^{\infty} sp(s)ds = 0$ ($E_S[s] = 0$).
2. $c \int_{-\infty}^{\infty} p(s)ds = c$ (Total probability is 1)
3. $\int_{-\infty}^a sp(s)ds = \int_{-\infty}^{\infty} sp(s)ds - \int_a^{\infty} sp(s)ds$
4. $\int_{-\infty}^a sp(s)ds = - \int_a^{\infty} sp(s)ds$ (since $\int_{-\infty}^{\infty} sp(s)ds = 0$).
5. $\int_{-\infty}^a = \Phi(a)$
6. $\int_a^{\infty} = (1 - \Phi(a))$

7.1. Signed Ray Distance Function

We will start with a signed ray distance function. The expected signed ray distance function is

$$E_S[d_{SR}(z; s)] = \int_{\mathbb{R}} (s - z)p(s)ds, \quad (17)$$

which can be rewritten as

$$\int_{\mathbb{R}} sp(s)ds - \int_{\mathbb{R}} zp(s)ds. \quad (18)$$

The first term is the expected value of S , or 0. The second term is $-z \int_{\mathbb{R}} p(s)ds$. Since $\int p(s)ds = 1$, this reduces to $-z$. This yields

$$E_S[d_{SR}(z; s)] = -z. \quad (19)$$

Alternately, one can recognize $S - z$ as normally distributed with mean $-z$, which has a mean of $-z$.

General form. The more general form of d_{SR} that accounts for the second intersection is done in two cases:

$$d_{SR'}(z; s) = \begin{cases} s - z & : z < s + n/2 \\ z - n - s & : z \geq s + n/2. \end{cases} \quad (20)$$

The expectation $E_S[d_{SR'}(z; s)]$ can be computed in two parts

$$\int_{-\infty}^{z - \frac{n}{2}} (z - n - s)p(s)ds + \int_{z - \frac{n}{2}}^{\infty} (s - z)p(s)ds. \quad (21)$$

For notational cleanliness, let $t = z - \frac{n}{2}$, and pull out constants and re-express any integrals as CDFs. Then the first integral expands to $z\Phi(t) - n\Phi(t) - \int_{-\infty}^t sp(s)ds$, and the second integral expands to $\int_t^{\infty} sp(s)ds - z(1 - \Phi(t))$. We

can then group and apply $\int_{-\infty}^t sp(s)ds = -\int_t^{\infty} sp(s)ds$, which yields $(2z - n)\Phi(t) - z + 2\int_t^{\infty} sp(s)ds$. A little re-arranging, and expanding out t yields:

$$E_S[d_{SR'}](z; s) = -z + (2z - n)\Phi\left(z - \frac{n}{2}\right) + 2 \int_{z - \frac{n}{2}}^{\infty} sp(s)ds. \quad (22)$$

This expression has $E_S[d_{SR}]$ in it ($-z$), plus terms (all but the first one) that activate once z approaches $\frac{n}{2}$.

7.2. Unsigned Ray Distance Function

The expected unsigned ray distance function is

$$E_S[d_{UR}(z; s)] = \int_{\mathbb{R}} |s - z|p(s)ds. \quad (23)$$

Before calculating it in general, we can quickly check what value the expected distance function takes on at the actual intersection by plugging in $z = 0$, or

$$E_S[d_{UR}(0; s)] = \int_{\mathbb{R}} |s|p(s)ds. \quad (24)$$

This integral evaluates to $\sigma\sqrt{2/\pi}$, which can be quickly obtained by noting that it is the expected value of a half-normal distribution. Indeed, the distribution over $d_{UR}(z; S)$ is a folded normal distribution with mean $-z$.

We can then derive the more general form, by calculating the integral in two parts: $E_S[d_{UR}(z; s)]$ is

$$\int_{-\infty}^z (z - s)p(s)ds + \int_z^{\infty} (s - z)p(s)ds. \quad (25)$$

We can expand and shuffle to yield

$$z \int_{-\infty}^z p(s)ds - z \int_z^{\infty} p(s)ds + \int_z^{\infty} sp(s)ds - \int_{-\infty}^z sp(s)ds. \quad (26)$$

The first two terms can be written in terms of the CDF Φ , and the last term can be further simplified by noting $\int_{-\infty}^z sp(s)ds = -\int_z^{\infty} sp(s)ds$. This yields a final form for $E_S[d_{UR}(z; s)]$,

$$z\Phi(z) - z(1 - \Phi(z)) + 2 \int_z^{\infty} sp(s)ds. \quad (27)$$

As seen before, when z is zero, the result is $\sigma\sqrt{2/\pi}$, which is the minimum. For $z \ll 0$, both $\Phi(z)$ and the integral can be ignored, leading a value of $\approx -z$. Symmetrically, the value is $\approx z$ if $z \gg 0$. Near zero, the function is more complex.

Derivative. The derivative of Equation 27 can be calculated out in three parts

$$\begin{aligned}\frac{\partial}{\partial z} z\Phi(z) &= zp(z) + \Phi(z) \\ \frac{\partial}{\partial z} z(1 - \Phi(z)) &= zp(z) - \Phi(z) + 1 \\ \frac{\partial}{\partial z} 2 \int_z^\infty sp(s)ds &= -2zp(z)\end{aligned}\quad (28)$$

Adding the first, subtracting the second, and adding the third yields the final result:

$$\frac{\partial}{\partial z} E_S[d_{UR}(z; s)] = 2\Phi(z) - 1. \quad (29)$$

In the tails, $\Phi(z)$ splits to 0 and 1, and thus $\frac{\partial}{\partial z} E_S[d_{UR}(z; s)]$ splits to -1 and 1. When z is not in the tail, the derivatives are not one.

General Form. The more general form of d_{UR} that accounts for the second intersection is

$$d_{UR'}(z; s) = \begin{cases} s - z & : z < s \\ z - s & : z > s, z - \frac{n}{2} < s \\ n - z & : z - \frac{n}{2} > s. \end{cases} \quad (30)$$

This can be computed in three parts. Again, let $t = z - \frac{n}{2}$ to reduce notational clutter. Then $E_S[d_{UR'}(z; s)]$ is

$$\begin{aligned}&\int_{-\infty}^t (n - z)p(s)ds + \\ &\int_t^z (z - s)p(s)ds + \\ &\int_z^\infty (s - z)p(s)ds.\end{aligned}\quad (31)$$

As usual, we pull out constants and rewrite integrals in terms of the CDF or 1 minus the CDF. This yields

$$\begin{aligned}&n\Phi(t) - z\Phi(t) + \\ &z(\Phi(z) - \Phi(t)) - \int_t^z sp(s)ds + \\ &\int_z^\infty sp(s)ds - z(1 - \Phi(z)).\end{aligned}\quad (32)$$

If we gather terms involving $\Phi(t)$ and $\Phi(z)$, as well as the integrals, we get

$$\begin{aligned}&(n - 2z)\Phi(t) + 2z\Phi(z) - z + \\ &- \int_t^z sp(s)ds + \int_z^\infty sp(s)ds.\end{aligned}\quad (33)$$

The value $-\int_t^z sp(s)ds = \int_{-\infty}^t sp(s)ds + \int_z^\infty sp(s)ds$, which lets us rewrite the integrals, yielding

$$\begin{aligned}&(n - 2z)\Phi(t) + 2z\Phi(z) - z + \\ &2 \int_z^\infty sp(s)ds + \int_{-\infty}^t sp(s)ds,\end{aligned}\quad (34)$$

where terms from the original URDF are highlighted in orange (note that $z\Phi(z) - z(1 - \Phi(z)) = 2\Phi(z) - z$). Rearranging, and re-substituting back in $t = z - \frac{n}{2}$ yields

$$\begin{aligned}&z\Phi(z) + -z(1 - \Phi(z)) + 2 \int_z^\infty sp(s)ds + \\ &(n - 2z)\Phi\left(z - \frac{n}{2}\right) + \int_{-\infty}^{z - \frac{n}{2}} sp(s)ds.\end{aligned}\quad (35)$$

Again, this is like $E_S[d_{UR}]$ but with additional terms (those in the second line) that activate once z approaches $\frac{n}{2}$.

7.3. Occupancy Ray Function

The standard occupancy function (i.e., positive is interior, negative is exterior) is not defined on non-watertight meshes. We can define an alternate occupancy function which is positive near a surface and negative away from a surface.

Specifically the expected occupancy function is

$$E_S[d_{ORF}(z; s)] = \int_{\mathbb{R}} \mathbf{1}_{\{x:|x-s| < r\}}(z)p(s)ds, \quad (36)$$

where $\mathbf{1}$ is the indicator function. Equation 36 can be simplified as

$$\int_{z-r}^{z+r} p(s)ds = \Phi(z+r) - \Phi(z-r). \quad (37)$$

7.4. Directed Ray Distance Function

We propose instead, to use

$$d_{DRDF}(z; s) = \begin{cases} s - z & : z \leq n/2 + s \\ n + s - z & : z > n/2 + s, \end{cases} \quad (38)$$

which switches over signs halfway to the next intersection. The expectation can be done the two cases. Let $t = z - \frac{n}{2}$ for clarity, then the expectation is

$$\int_{-\infty}^t (n + s - z)p(s)ds + \int_t^\infty (s - z)p(s)ds. \quad (39)$$

These can be broken, grouped by content of the integrals, and had constants pulled out to produce

$$\begin{aligned}&n \int_{-\infty}^t p(s)ds + \\ &\int_{-\infty}^t sp(s)ds + \int_t^\infty sp(s)ds + \\ &-z \int_{-\infty}^t p(s)ds - z \int_t^\infty p(s)ds.\end{aligned}\quad (40)$$

From here, one can rewrite the first line as $n\Phi(z - \frac{n}{2})$. The second line is 0, since it groups to be $\int_{\mathbb{R}} sp(s)ds = 0$. The

third line is $-z$, since the integrals group to cover all the reals, and $\int_{-\infty}^{\infty} p(s)ds = 1$. This leaves the final result

$$E_S[d_{\text{DRDF}}(z; s)] = n\Phi\left(z - \frac{n}{2}\right) - z \quad (41)$$

The derivative of this expression is

$$\frac{\partial}{\partial z} E_S[d_{\text{DRDF}}(z; s)] = np\left(z - \frac{n}{2}\right) - 1 \quad (42)$$

because $\frac{\partial}{\partial z}\Phi(z) = p(z)$. This expression is -1 unless $np(z - \frac{n}{2})$ is large.

7.5. Planes

We are given a plane consisting of a normal $\mathbf{n} \in \mathbb{R}^3$ with $\|\mathbf{n}\|_2 = 1$ and offset o (where points \mathbf{x} on the plane satisfy $\mathbf{n}^T \mathbf{x} + o = 0$). Our uncertainty about the plane's location in 3D is $\mathbf{s} \sim N(\mathbf{0}, \sigma^2 \mathbf{I})$ where \mathbf{I} is the identity matrix and $\mathbf{0}$ a vector of zeros. Then $d_U(\mathbf{x}; \mathbf{s})$ is the 3D unsigned distance function

$$d_U(\mathbf{x}) = |\mathbf{n}^T \mathbf{x} + o|. \quad (43)$$

We will then compute the expected distance

$$E_{\mathbf{s}}[d_U(\mathbf{x}; \mathbf{s})] = \int_{\mathbb{R}^3} |\mathbf{n}^T(\mathbf{x} + \mathbf{s}) + o| (\mathbf{s}) ds. \quad (44)$$

First, note that we are free to pick the coordinate system, and so we pick it so that the plane passes through the origin and is perpendicular to the z -axis. Thus, $\mathbf{n} = [0, 0, 1]$ and $o = 0$. This does not require the plane to be perpendicular to the ray; this is merely placing the arbitrary coordinate system to be in a mathematically convenient configuration. Geometrically, this is precisely identical to the ray case: any uncertainty that is perpendicular to the plane does not alter the distance to the plane, leaving a single source of uncertainty (in z).

Algebraically, one can verify this as well. The distance to the plane for any point \mathbf{x} is $|\mathbf{n}^T \mathbf{x} - o|$. We can add the uncertainty about the plane's location by subtracting it off the point, placing the point at $\mathbf{x} - \mathbf{s}$. Then the distance is $|\mathbf{n}^T(\mathbf{x} - \mathbf{s}) - o|$. Since $\mathbf{n} = [0, 0, 1]$ and $o = 0$, this simplifies to $|\mathbf{x}_z - \mathbf{s}_z|$, where \mathbf{x}_z is the z coordinate of \mathbf{x} and likewise for \mathbf{s}_z . The final expected value of the 3D distance is

$$\iint_{\mathbb{R}^2} \left(\int_{-\infty}^{\infty} |\mathbf{x}_z - \mathbf{s}_z| p(\mathbf{s}_z) ds_z \right) p(\mathbf{s}_x)p(\mathbf{s}_y) d\mathbf{s}_x d\mathbf{s}_y. \quad (45)$$

Since the inner integral is constant with respect to \mathbf{s}_x and \mathbf{s}_y , we can pull it out; we can also rewrite $|\mathbf{x}_z - \mathbf{s}_z|$ as $|\mathbf{s}_z - \mathbf{x}_z|$ to match convention, yielding:

$$\left(\int_{-\infty}^{\infty} |\mathbf{s}_z - \mathbf{x}_z| p(\mathbf{s}_z) ds_z \right) \iint_{\mathbb{R}^2} p(\mathbf{s}_x)p(\mathbf{s}_y) d\mathbf{s}_x d\mathbf{s}_y. \quad (46)$$

The right double integral is 1, leaving the expected unsigned distance function

$$\int_{-\infty}^{\infty} |\mathbf{s}_z - \mathbf{x}_z| p(\mathbf{s}_z) ds_z. \quad (47)$$

A few things follow from this setup. First, the minimum value at the real intersection will still be $\sigma\sqrt{2/\pi}$. Second, the only uncertainty that matters is the variance in the direction perpendicular to the plane: if $s \sim N(\mathbf{0}, \text{diag}[\sigma_x^2, \sigma_y^2, \sigma_z^2])$, then only σ_z^2 controls the distortion of the UDF. Finally, the expected distance along a ray that is not perpendicular to the plane be stretched proportionally to the cosine between the ray and the normal. Thus, the qualitative behavior (i.e., where the sign of the derivative changes) will be similar, but the rate at which things change will not be.

References

- [1] Matan Atzmon and Yaron Lipman. Sal: Sign agnostic learning of shapes from raw data. In *Proceedings of the IEEE/CVF Conference on Computer Vision and Pattern Recognition*, pages 2565–2574, 2020. [2](#)
- [2] Angel Chang, Angela Dai, Thomas Funkhouser, Maciej Halber, Matthias Niessner, Manolis Savva, Shuran Song, Andy Zeng, and Yinda Zhang. Matterport3d: Learning from rgb-d data in indoor environments. *arXiv preprint arXiv:1709.06158*, 2017. [1, 2, 3, 10](#)
- [3] Julian Chibane, Aymen Mir, and Gerard Pons-Moll. Neural unsigned distance fields for implicit function learning. In *Advances in Neural Information Processing Systems (NeurIPS)*, December 2020. [2](#)
- [4] Angela Dai, Angel X Chang, Manolis Savva, Maciej Halber, Thomas Funkhouser, and Matthias Nießner. Scannet: Richly-annotated 3d reconstructions of indoor scenes. In *Proceedings of the IEEE Conference on Computer Vision and Pattern Recognition*, pages 5828–5839, 2017. [2, 3, 10, 15](#)
- [5] Huan Fu, Bowen Cai, Lin Gao, Lingxiao Zhang, Cao Li, Qixun Zeng, Chengyue Sun, Yiyun Fei, Yu Zheng, Ying Li, Yi Liu, Peng Liu, Lin Ma, Le Weng, Xiaohang Hu, Xin Ma, Qian Qian, Rongfei Jia, Binqiang Zhao, and Hao Zhang. 3d-front: 3d furnished rooms with layouts and semantics. *arXiv preprint arXiv:2011.09127*, 2020. [2, 3, 10, 13](#)
- [6] Steven M Seitz, Brian Curless, James Diebel, Daniel Scharstein, and Richard Szeliski. A comparison and evaluation of multi-view stereo reconstruction algorithms. In *2006 IEEE computer society conference on computer vision and pattern recognition (CVPR'06)*, volume 1, pages 519–528. IEEE, 2006. [1](#)
- [7] Maxim Tatarchenko, Stephan R Richter, René Ranftl, Zhuwen Li, Vladlen Koltun, and Thomas Brox. What do single-view 3d reconstruction networks learn? In *Proceedings of the IEEE Conference on Computer Vision and Pattern Recognition*, pages 3405–3414, 2019. [1](#)